DIFFUSION IN DYE-SENSITIZED SOLAR CELLS

PORE-SIZE DEPENDENCE OF ION DIFFUSIVITY IN DYE-SENSITIZED SOLAR CELLS

By YIQUN MA, B.ENG.

A Thesis Submitted to the School of Graduate Studies in Partial Fulfillment of

the Requirements for the Degree Master of Applied Science

McMaster University

MASTER OF APPLIED SCIENCE (2013)	McMaster University
(Materials Science and Engineering)	Hamilton, Ontario

TITLE:	Pore-size Dependence of Ion Diffusivity in Dye-sensitized Solar Cells
AUTHOR:	Yiqun Ma, B. Eng. (National University of Singapore)
SUPERVISOR:	Professor Gu Xu
NUMBER OF PAGES:	xi, 89

ABSTRACT

The pore-size dependence of liquid diffusivity in mesopores has been a controversial topic. It is especially meaningful in dye-sensitized solar cells (DSSCs) because the triiodide ion diffusivity is closely related to the cell performance. By applying electrochemical measurements, the pore-size dependence of ion diffusivity in DSSCs was investigated based on TiO_2 thin films of variable pore diameters. The alternation of pore-size was achieved by the epitaxial growth of TiO_2 after $TiCl_4$ post-treatments. From the trend of normalized diffusivities, the respective valid regimes of pore-size dependent and independent diffusion were determined, which were separated by the transition point located at 5-7 nm. In addition, my results have showed that the DSSC fabrication processes, e.g., dye loading, $TiCl_4$ post-treatment will not lead to the transition of diffusion behaviors. Furthermore, the unexpected drop of diffusivity after one $TiCl_4$ treatment is attributed to the involvement of surface diffusion in untreated TiO_2 matrix.

ACKNOWLEDGEMENT

First of all, I would like to express my gratitude to my supervisor Dr. Gu Xu, for providing me this opportunity to explore in the area of dye-sensitized solar cells. I also thank for his patience and guidance when I encountered difficulties.

I would like to thank my group members, Cindy Zhao, Lucy Deng, Kewei Wang, Han Yan for their assistance and support throughout the my research, and for the enlightening group discussions.

The technicians and staff members in the department, Doug, Ed, Xiaogang, Diana, Nanci, and Jane, all of them have also warmly provided me help whenever I needed. I really appreciate it.

Last but not least, I would like to thank my dear parents in China, for supporting me from oversea, encouraging me whenever I feel down, giving me advice whenever I feel confused. I am deeply grateful for them and always will be.

CONTENTS

LIST OF FIGURES

LIST OF TABLES

---

1 INTRODUCTION

1.1 SOLAR ENERGY AND SOLAR CELLS

The advancement of human society depends on the availability of energy source. Nowadays, the shortage of energy is a global problem which requires immediate attentions. Our world will need at least 10 Terawatts of additional energy from clean and low-cost energy source by 2050 to maintain worldwide peace and prosperity [1]. Solar energy is one promising source of clean energy with adequate supply, i.e., 3 million exajoules per year. The current energy demand can be fully met by covering 0.15% of earth's surface with 10% efficiency solar cell panels [2].

1.1.1 Brief History of Solar Cells

Solar cells, also known as photovoltaic, can be generally referred to all devices which convert solar energy directly/indirectly into electric energy, and the phenomenon of this conversion from photons to electricity is known as the photovoltaic effect. Surprisingly, it was first observed in a liquid phase electrochemical cell in 1839 by Alexandre-Edmond Becquerel. The first solid state photovoltaic device was developed by William Adams and Richard Day in 1876. It was made of selenium and platinum in the structure of Pt/Se/Pt. Au/Se/M system was used by Charles Fritts in 1894. It is interesting that the early attempts were all using the Schottkey junction (metal/semiconductor) while the theory was not developed until 1930s.[3]

The usage of semiconductor materials, mostly silicon, was limited by the purification and manufacture of high quality silicon. Semiconductors are well known to be extremely sensitive to impurities. The first silicon p-n junction solar cell was fabricated at Bell Labs by D.M. Chapin, C.S. Fuller and G.L. Pearson in 1954 [4]. This is about the same time as emergence of semiconductor transistor and integrated circuit technologies. Other types of p-n junction solar cells, including cadmium sulfide (CdS), indium phosphide (InP), cadmium telluride (CdTe) devices, were initially studied in the 1950s too.

The great leap in photovoltaic devices happened in the 1970s, driven by the energy crisis which lead to intensive research and development of clean energy sources. The fundamental understanding of modern photovoltaic science was developed and rooted mainly in that period.

In the present, the most successful and mature photovoltaic material is unquestionably silicon. The development of silicon solar cells is greatly benefitted from the advancement of microelectronic industry which requires high quality silicon wafers. The production quality and efficiency has made silicon the foremost solar cell material. The performance of the test silicon solar cells has advanced very close to the theoretical limit of 29% [5]. The commercialized silicon solar cells also have high power conversion efficiency (PCE) of 16% - 24%, together with excellent stability [6]. However, since high purity single crystal silicon is required, the main challenge is to further lower the manufacture cost to meet the demand of mass production.

1.1.2 Basic Physics of Solar Cells

Despite of the difference in materials and designs, most solid state/quasi-solid state semiconductor photovoltaic devices share a similar working principle in general. The following diagram (**Fig.** 1.1) illustrates the general working physics of most semiconductor solar cells. There are mainly three steps, i.e., 1. Light adsorption; 2. Exciton generation; 3. Charge separation.

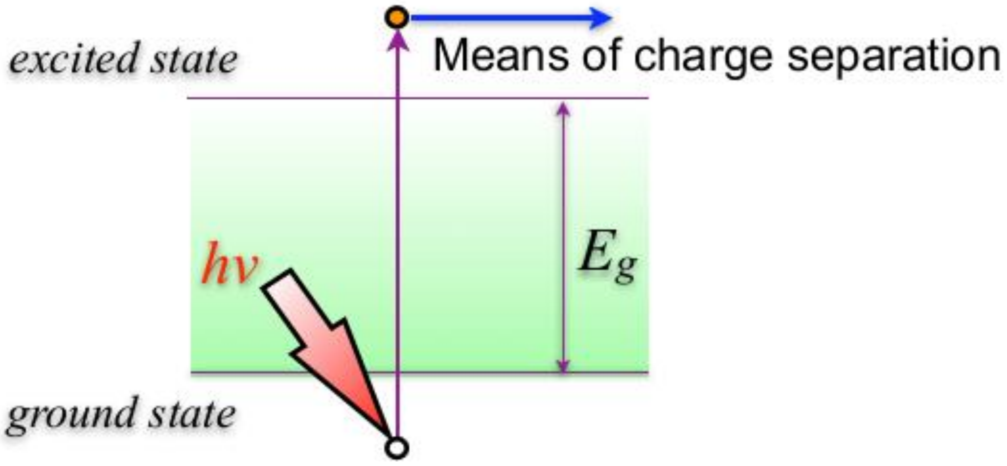

Figure 1.1: Basic working principle of semiconductor based solar cells

It is against the physics laws for this conversion process to have 100% efficiency. The theoretical maximum of power conversion efficiency is restricted by thermodynamic limits, because this conversion process is irreversible occurring under non-equilibrium conditions [7]. The loss of energy can be divided into:

1. Power extraction from the solar cell device is an irreversible process. Thus there is a loss of free energy ΔG due to non-equilibrium conditions at maximum power extraction. $\eta_1 \approx 0.91$ (considering incoming photon energy $\approx$1eV).
2. Carnot efficiency limit due to the finite temperature difference between photons and the device. The temperature of the monochromatic diffuse radiation in all direction is defined as the temperature of a black body give rise to the same irradiance at the wavelength. The maximum conversion efficiency is given by $\eta_2 = (T_{ph} - T_{sc})/T_{ph} \approx 0.77$ under AM 1.5 condition.

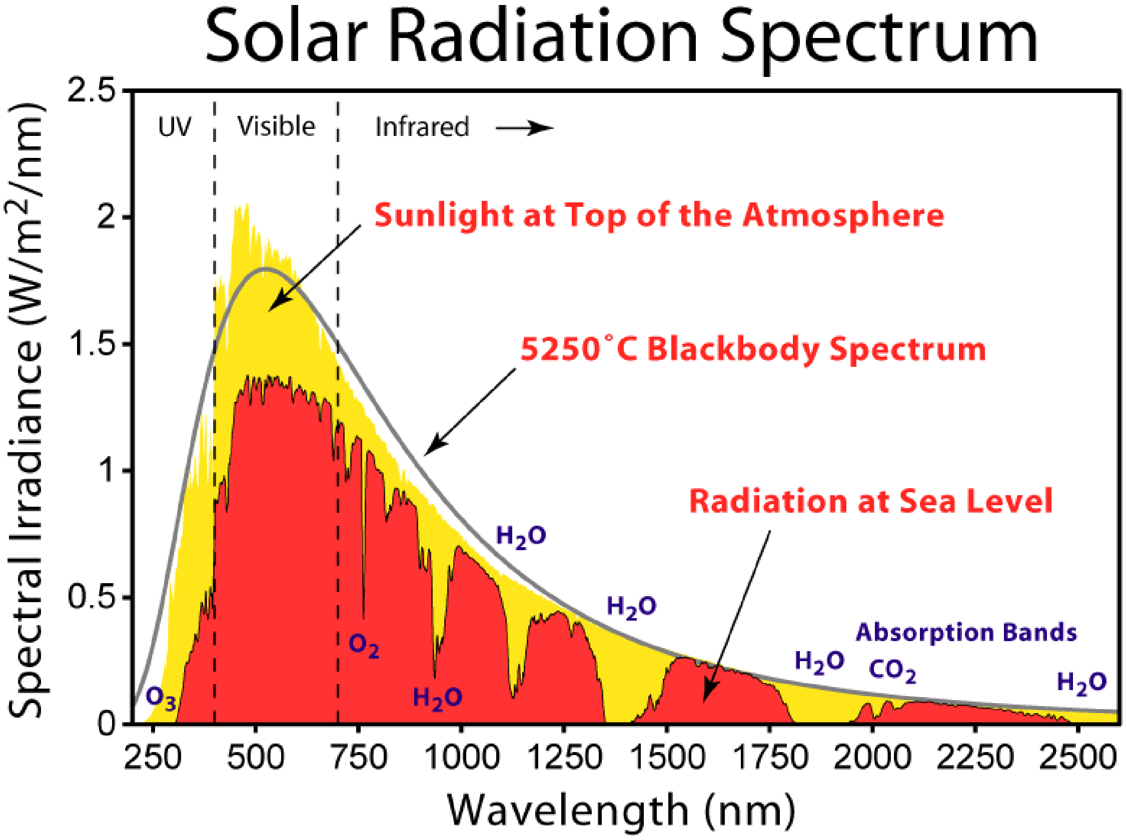

Figure 1.2: Solar radiation spectrum

3. Sunlight is not a monochromatic radiation. The solar spectrum is given in **Fig.** 1.2, showing the peak region of solar energy is in the visible light range. For a single band gap semiconductor, photons with energy lower than the band gap will not be absorbed, while the excessive energy of photons with higher energy than the band gap would be wasted. (**Fig.** 1.3) The relaxation of high energy excitons happens instantaneously and the excessive energy will be dissipated as heat. The maximum efficiency $\eta_3 \approx 0.48$ when band gap = 1.34eV.

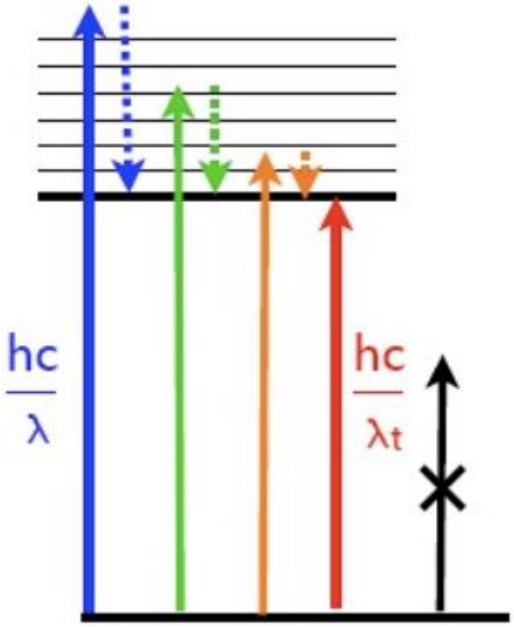

Figure 1.3: Excitation and relaxation conditions of photons with different energy

Combining all these factors above gives the Shockley–Queisser limit (**Fig.** 1.4), which is the theoretical efficiency limit of a single band gap semiconductor solar cell [8]. The maximum value of $\eta = \eta_1 \cdot \eta_2 \cdot \eta_3 \approx 33.7\%$. The major loss is due to the spectrum loss of polychromatic radiation. This limit can be overcome by using multiple band gap design in some new generation solar cells.

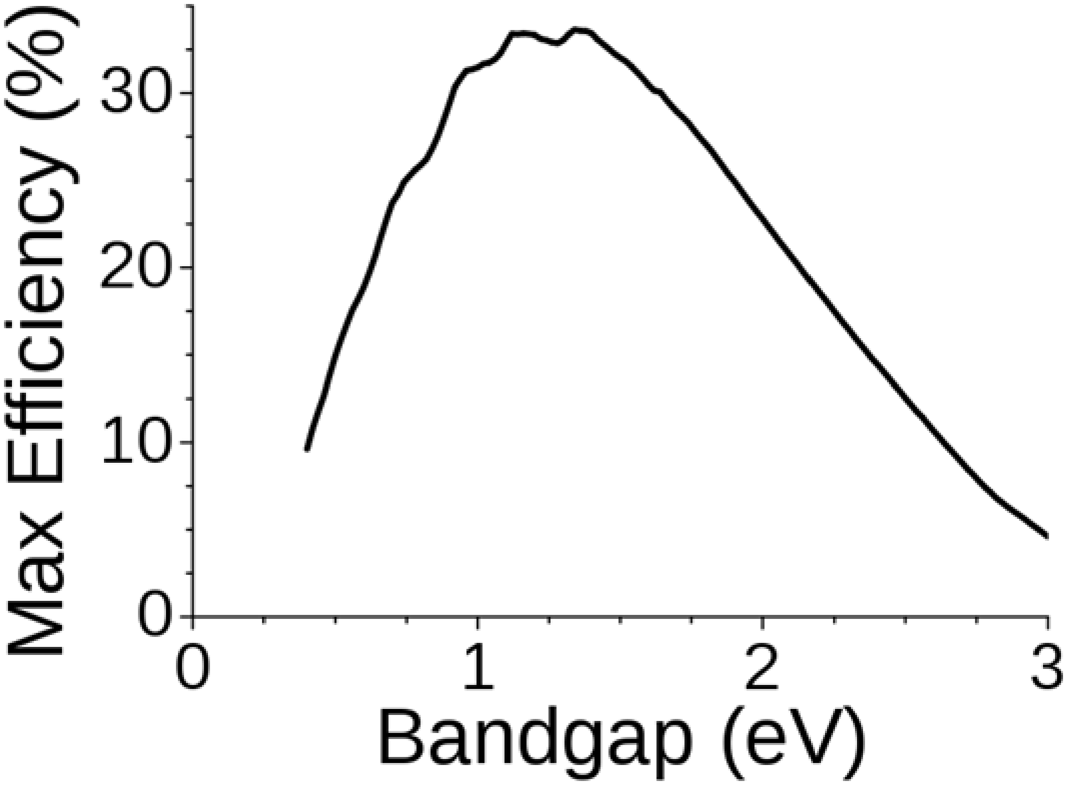

Figure 1.4: The Shockley–Queisser limits of single band gap photovoltaics

1.1.3 Classifications of Solar Cells

There are many ways to classify the solar cells into different categories. From the development point of view, solar cells can be put into first generation, second generation and third generation cells. First generation solar cells are made from single crystal inorganic semiconductors, such as silicon (Si), gallium arsenide (GaAs), indium phosphide (InP), that have high power conversion efficiencies but extremely high manufacture cost because single crystal material is used. Second generation solar cells refer to the inorganic thin film solar cells. The representatives in this group include amorphous silicon (a-Si), cadmium telluride (CdTe), copper indium gallium di-selenide (CIGS), copper zinc tin sulfide (CZTS) as well as organic/hybrid thin film cells. The inorganic solar cells have satisfactory PCEs and much lower cost compared to first generation solar cells. However, restricted by the requirement of the heavy elements, it becomes difficult to further lower the cost of inorganic solar cells. Therefore, people try to develop organic and hybrid solar cells in order to replace those inorganic elements. They are promising solar cells with possible low cost and facile fabrication methods in the future. However, due to the intrinsic nature of organic materials, organic solar cells usually suffer from low charge carrier mobility and stability issues [9]. Therefore, a lot of work still needs to be done.

The third generation solar cells are devices with frontier technology in the aim of breaking the thermodynamic limit introduced earlier. Concentrator solar cells utilize optical devices to concentrate the incoming sunlight into a spot, so as to increase the effective temperature of the incident radiation. Thus the Carnot efficiency can be further raised. However, the main purpose of concentrator solar cell is to reduce the amount of active material required and thus lower the cost [10].

According to the calculation in Section 1.1.2, the major limitation of efficiency originates from the spectrum loss of polychromatic nature of sunlight. There have been many innovative attempts to overcome the barrier. One straightforward solution is use multi-layer semiconductor materials with different band gap, which is known as tandem cells or multi-junction cells. This type of solar cell has successfully pushed the PCE to over 40% [11]. However, the high material cost associated with the cell limited its application only in cost-insensitive areas such as in space satellites.

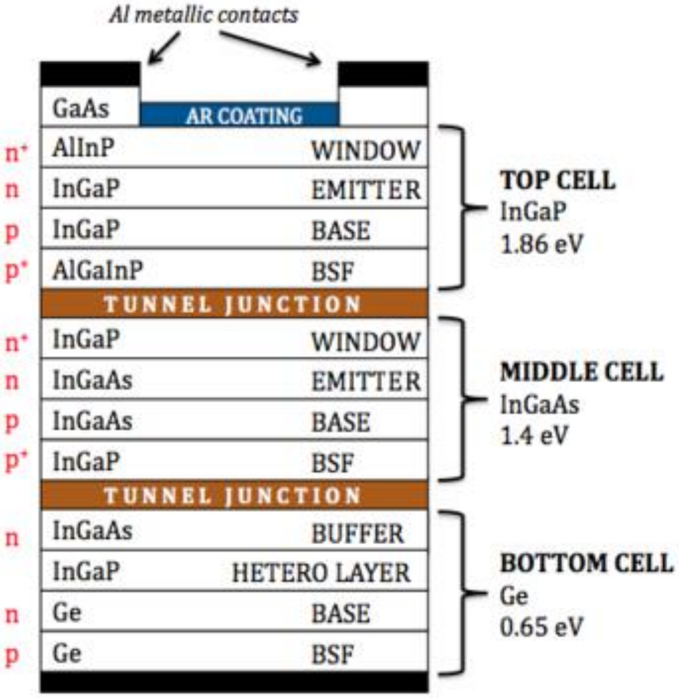

Figure 1.5: Structure of a multi-junction solar cell [12]

Other noteworthy mechanisms include phonon bottleneck for slow cooling of energetic excitons [13], multiple exciton generation from single photon [14], and spectrum conversion of incident light. However, many of these ideas are still in their infancy stage. A lot of scientific and technical issues need to be resolved before producing practically useful solar cells.

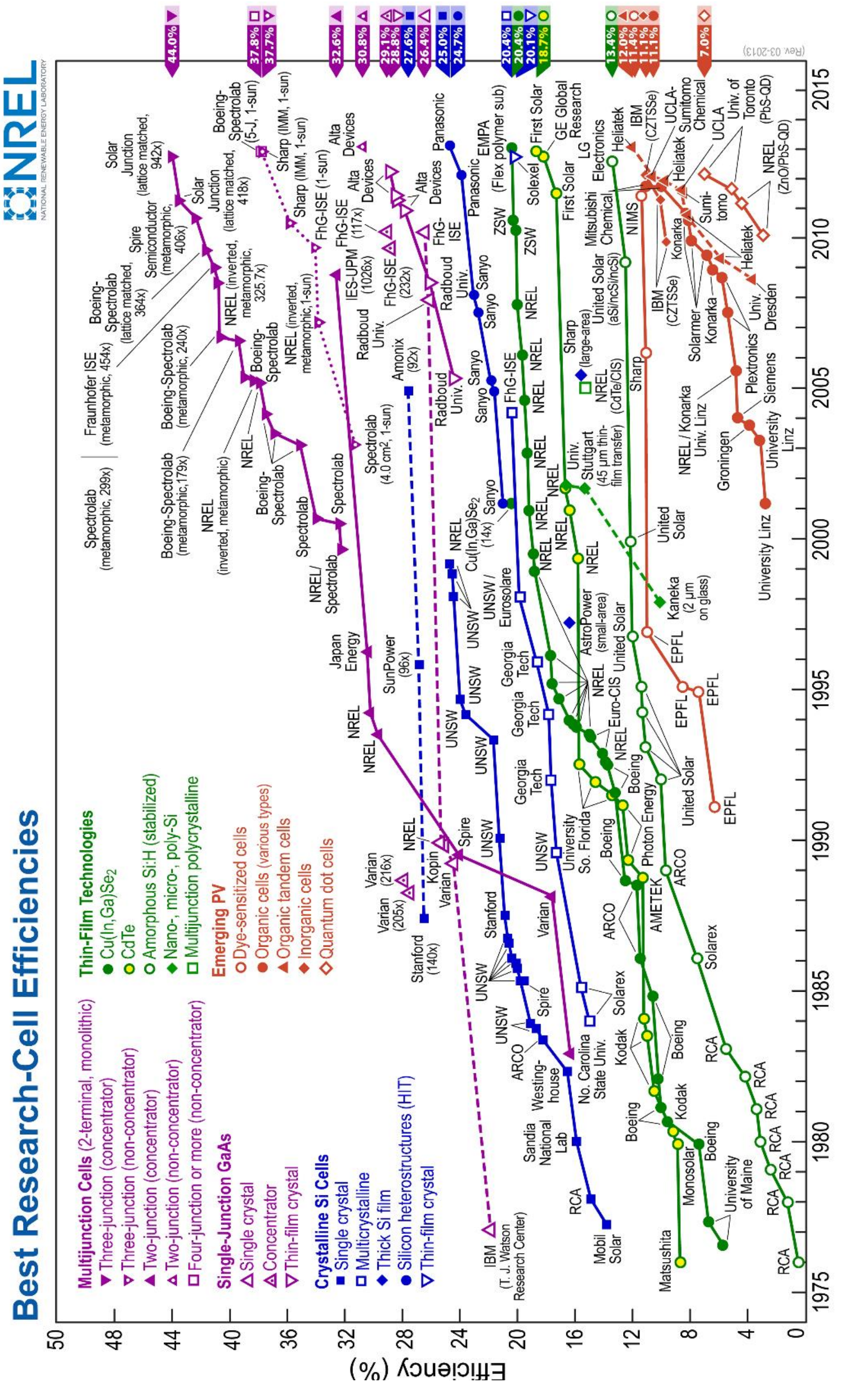

Figure 1.6: Best research cell efficiencies recorded by national renewable energy laboratory (NREL) [15]

1.2 DYE-SENSITIZED SOLAR CELLS

Now the term ‘dye-sensitized solar cell’ (DSSC) usually refers to the Grätzel’s cell which is indubitably the most promising type of the dye-sensitized solar cells. It is considered as one of the second generation hybrid solar cells which consists of both organic and inorganic materials. Dye-sensitized solar cells were first invented and published in Nature in 1991 [16]. The power conversion efficiency in the original publication was 7%. After more than two decades of development, the efficiency has now exceeded 12% [17].

1.2.1 Device Structure of Dye-sensitized Solar Cells

A typical DSSC is made of a large band gap porous layer semiconductor as photoanode, and liquid electrolyte as a mediator between the metal-oxide and counter electrode [18]. The electrochemical junction formed at the semiconductor/electrolyte interface assists the charge separation process. The phrase ‘dye-sensitized’ means that the sunlight is mainly harvested by the monolayer of dye molecules which are loaded on the surface of metal-oxide porous thin film. Transparent conducting material, e.g., fluorine doped tin oxide (FTO) glass, is used as the substrate metal oxide film to ensure minimum sunlight blocking and efficient charge transport to the outer circuit. Catalyst materials of the redox reaction, e.g., platinum, carbon, are coated on the counter electrode to minimize charge transfer resistance. **Fig.** 1.7 is a schematic drawing of a typical DSSC. The main advantages of DSSCs are good efficiency, excellent stability and economical manufacturing processes.

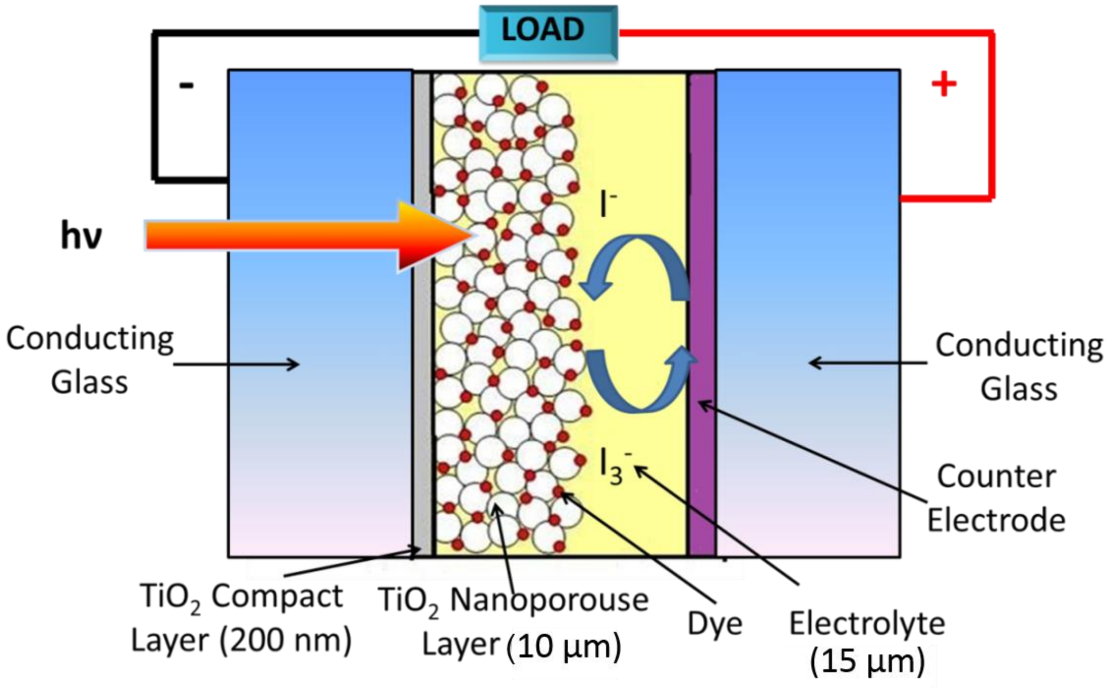

Figure 1.7: Structure of a dye-sensitized solar cell [19]

1.2.2 Materials of Dye-sensitized Solar Cells

After the initial publication in 1991, dye-sensitized solar cells have attracted immense research interest. Numerous attempts have been made to replace parts of the original design with different materials for the purpose of further improving the cell efficiency.

Metal-oxide Semiconductor

For the semiconductor layer, other wide band gap metal oxide semiconductors have been tested, including, SnO_2, ZnO, Nb_2O_5, $SrTiO_3$, NiO etc. In spite of some of the materials having superior electronic properties to TiO_2, e.g., ZnO has much higher electron mobility [20], It is surprising that TiO_2 still gives almost the best performance and stability thus far. Meanwhile, NiO is the most successful p-type semiconductor used in DSSCs [21], with efficiency slightly lower than n-type DSSCs.

Dye sensitizers

The function of the dye molecules is to capture sunlight and inject the electron into the semiconductor. Therefore, an ideal choice of dye molecules should satisfy the following criteria,

1. The energy gap between the lowest unoccupied molecular orbital (LUMO) and the highest occupied molecular orbital (HOMO) should be close to the ideal band gap of 1.34 eV.
2. The positions of LUMO and HOMO should be compatible with the band positions of the semiconductor and redox energy level for efficient charge transfer.
3. The dye molecules should be readily oxidized and reduced with good chemical stability at the same time.

Currently, the most successful dye species used is ruthenium based dye, mainly because of broad adsorption spectra and rapid charge injection rates [22]. Although black dye would have the best light harvesting property, dyes with various colors have been used in practical cells for aesthetic reasons (**Fig.** 1.8).

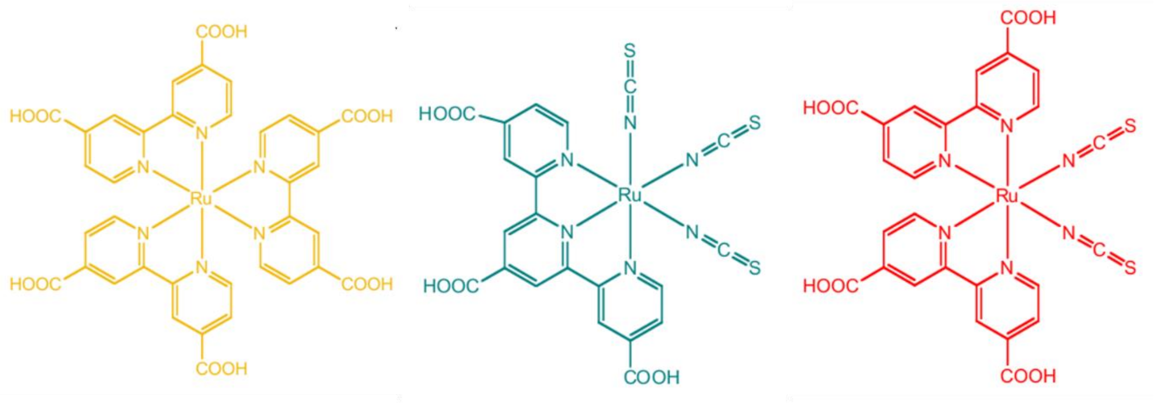

Figure 1.8: Molecular structures of dye molecules with different colors

Electrolyte

The function of electrolyte is acting as a mediator between the dye molecules and the counter-electrode. Considering the working conditions of dye-sensitized solar cells, the electrolyte is required to be chemically and thermally stable at elevated temperature under sunlight radiation. This is particularly a challenge for liquid electrolyte using volatile organic solvent. Furthermore, due to the mesoporous nature of the semiconductor photo anode, the electrolyte should absorb minimum amount of light so that the photons can pass through the electrolyte and reach the dye molecules. The common examples of redox couples are I^-/I_3^-, Br^-/Br_2, SCN^-/SCN_2, and metal ion based complexes such as cobalt complex and copper complex.

Researchers also tried to replace the liquid electrolyte with solid/quasi-solid electrolyte/mediator to avoid the evaporation and leaking problems. Comprehensive studies have been carried out on both inorganic (CuI, CuSCN) [23] and organic (spiro-

MeOTAD) hole conductors [24]. The problem of solid electrolytes is often the poor contact at the interface and incomplete infiltration into nanoscale mesopores [25].

1.2.3 Operation Principles of Dye-sensitized Solar Cells

The operation principles can be illustrated based on the energy band structure of the whole device (**Fig.** 1.9). The example shown here is the most classic design of DSSCs which uses titanium dioxide (TiO_2) as semiconductor and the I^-/I_3^- redox couple as liquid electrolyte. When sunlight enters the device through FTO (F: SnO2) glass, the photons will be absorbed by the monolayer dye molecules and excite them into excited states. After that, the excited dye molecules (S^*) will inject electrons into the conduction band (CB) of TiO_2, and become oxidized (S^+). Electrons transport through the porous TiO_2 layer and reach the FTO electrode. At the same time, the redox couple (D^+/D) in the electrolyte act as a mediator which transfers negative charges from the counter-electrode to oxidized dye molecules (S^+), and reduce them back to their original status (S). This forms the complete cycle of electron flow. The theoretical maximum open circuit voltage of DSSCs is the difference between Fermi levels of the metal oxide and redox couple.

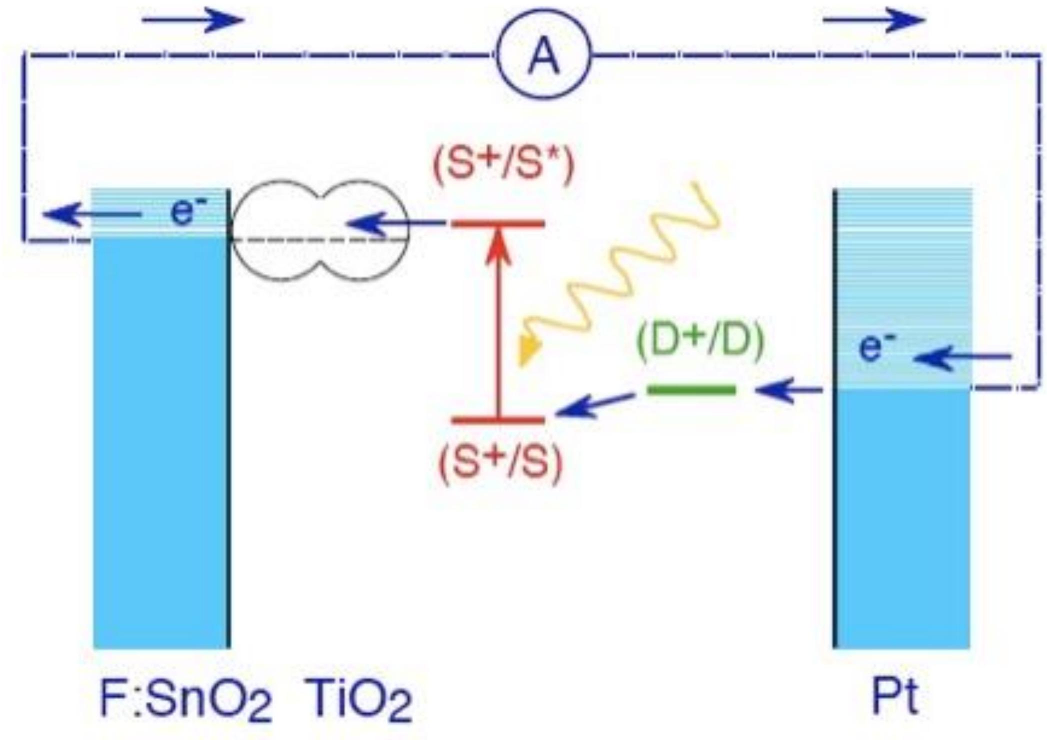

Figure 1.9: Schematic illustration of working principle of a standard dye-sensitized solar cell

1.3 MASS TRANSPORT OF IONS IN ELECTROLYTE

Mass transport of ions in the electrolyte is an important step in the working process of DSSCs. The mass transport rate is reflected as the mass transport limited current density of the electrolyte, which is the maximum current density the electrolyte can provide from mass transport processes. It is often the limiting factor of overall performance of DSSCs in many cases [26-28]. In order to optimize the cell design and further improve the cell efficiency, it is important to understand the mass transport process.

There are mainly three mechanisms for mass transport of ions in the liquid electrolyte, including diffusion, migration and convection [29]. A Grotthuss-like mechanism was also observed in some systems using a molten salt electrolyte which has extremely high ion strength, but it is generally absent in conventional systems with dilute solution [30].

1.3.1 Diffusion

There are two different types of diffusion phenomena, transport diffusion and self-diffusion. Transport diffusion is the mass transport process driven by a concentration gradient. Self-diffusion is due to the Brownian motion of molecules. The two processes are driven by essentially the same micro-dynamic mechanism, but the diffusivity of these two process may not necessarily be the same [31]. Since this study is about the mass transport of ions in electrolyte, only transport diffusion would be considered here.

As shown in **Fig.** 1.10, the rate of transport diffusion can be determined from the net flux of molecules. In contrast, the rate of self-diffusion is difficult to be measured macroscopically. It can only be tracked by determining the mean square displacement of a large amount of individual diffusing species.

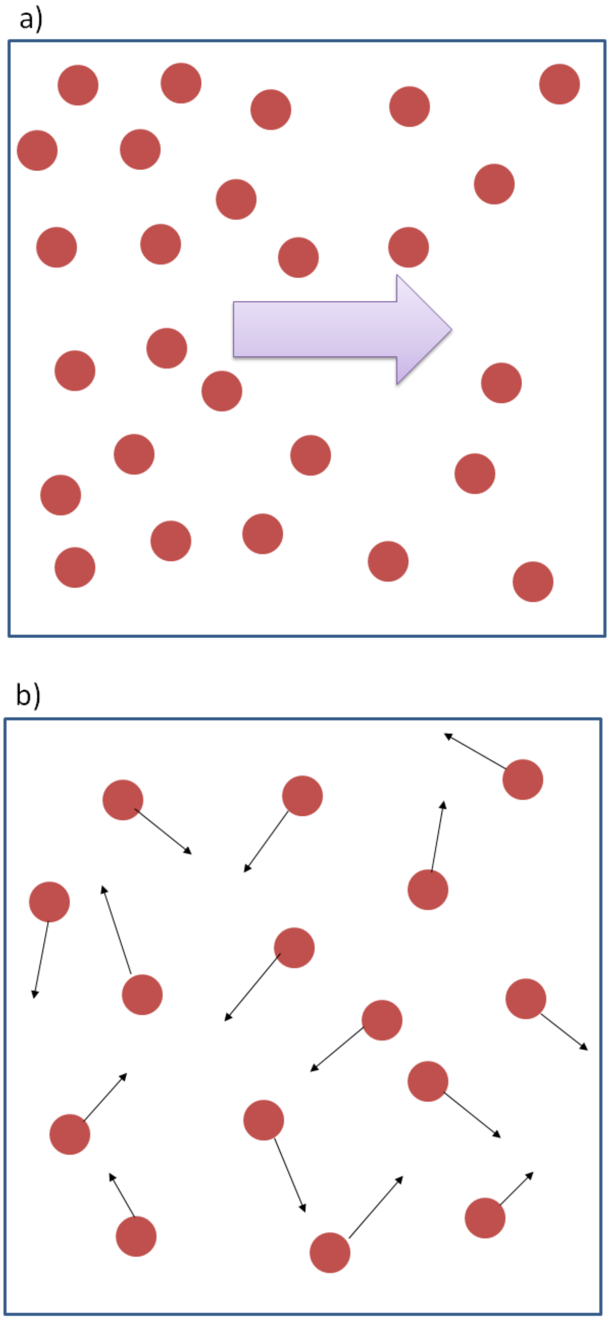

Figure 1.10: Different diffusion mechanisms of a) transport diffusion and b) self-diffusion

The transport diffusion coefficient can be derived from the Stoke-Einstein equation, with the assumption of spherical molecules.

$$D = \frac{kT}{6\pi\eta r} \qquad (1.1)$$

where η is the viscosity of the liquid, r is the hydrodynamic radius of the diffusing species. The relation shows that the diffusion coefficient is heavily related to the viscosity of the liquid. This is the reason of choosing low viscosity organic solvent in DSSCs.

The relationship between diffusion flux and concentration gradient is governed by the Fick's first law:

$$J_{flux} = D\frac{dC}{dx} \qquad (1.2)$$

And converting flux to current density:

$$J_{current} = nFD\frac{dC}{dx} \qquad (1.3)$$

where n is the stoichiometry constant, which equals 2 for I^-/I_3^- redox couple; F is the Faraday constant.

1.3.2 Other Mass Transport Mechanisms

Migration

Migration refers to the movement of ions resulting from an external electric field, which is governed by Coulomb's Law,

$$F = eE \tag{1.4}$$

However, the migration effect plays a limited role in the mass transport of ions in standard dye-sensitized solar cells. The electric field in the solution is less than the potential difference applied on the device, because of the series resistance of electrodes and connecting wires. Moreover, the presence of large amounts of I^- and Na^+ suppress the effect of electric field to the minority ions which is the I_3^- ion. [29]

Convection

Convection refers to the bulk liquid movement of substance caused by temperature difference or gravitational force. These external factors will lead to a change in relative buoyancy in different parts of the bulk liquid. In the case of dye-sensitized solar cell, convection is negligible due to the tiny spacing between the electrodes (≈25 μm) [29]. The temperature difference throughout the device is usually insignificant.

Grotthuss-like Mechanism

The Grotthuss-like mechanism was observed and confirmed in ionic liquid electrolyte in dye-sensitized solar cells in the past few years [32]. It is named Grotthuss-like because the mechanism bears significant similarity to the famous Grotthuss mechanism of proton transport in water. It is a bond exchange mechanism between a proton and water molecules [33], illustrated in **Fig.** 1.11. The proton first forms a hydrogen bond with nearby water molecules, followed by the cleavage of one covalent bond between the oxygen atom and one of the hydrogen atoms. A new proton will be formed with a net displacement with respect to the original proton. Therefore, the charge is transported in the water molecule network without bulk movement of the molecules.

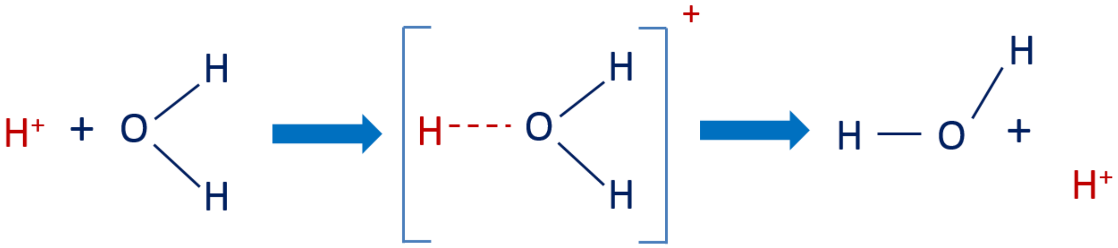

Figure 1.11: Illustration of proton exchange process in the Grotthuss mechanism

Similar processes can happen in the ionic liquid electrolyte of the I^-/I_3^- redox couple, shown in **Fig.** 1.12. This can enhance the overall charge transport rate in the electrolyte. At the same time, it might act as a confounding factor when determining the diffusion coefficient of ions from the mass transport limited current [34]. However, from the working mechanism of this bond exchange process, it is certain that this process can only occur in the presence of high concentration of acceptor molecules/ions. In this study, a dilute solution of the I^-/I_3^- redox couple (0.3M I^- and 0.03M I_3^-) is used as the test electrolyte. Thus, the Grotthuss-like mechanism is absent in the measurements.

Figure 1.12: The Grotthuss-like mechanism in a highly concentrated (ionic liquid) electrolyte based on I^-/I_3^- redox couple

1.3.3 Diffusion in Dye-sensitized Solar Cells

To conclude the arguments above, in the standard system of dye-sensitized solar cells with I^-/I_3^- redox couple in acetonitrile solvent, diffusion is the dominant mechanism. In addition, since the concentration of I^- is one order of magnitude greater than the concentration of I_3^-, and they have similar diffusivities [30], the overall diffusion rate is determined by the diffusion of I_3^-ions. Therefore, the overall mass transport rate of ions in electrolyte can be simplified into the diffusion rate of the minority ion in the redox system, which is the triiodide ions in this case.

However, the situation becomes complex with the presence of mesoporous metal oxide thin film. In general, mesopores refer to pores ranging in size from 2-50 nm [35]. The size of the pores in dye-sensitized solar cells usually range from 5 nm all the way to 20 nm, depending on the system [30]. The ions have to diffuse through those mesopores to reach all the dye molecules on the surface of the photoanode for dye recovery. There are a few theories regarding the liquid diffusion in mesopores based on experimental observations, but with controversial views in certain ranges.

1.4 RESEARCH OBJECTIVES

As mentioned above, the limiting current of electrolyte is often the bottleneck of the overall cell device. Thorough understanding of the diffusion behavior, especially the liquid molecule diffusion in mesopores, is crucial for the further improvement of the device performance of dye-sensitized solar cells. It is known that the diffusivity will be affected by the various physical/chemical properties of the thin film, for example pore structure, pore size, surface tension and so on. There have been previous studies in this area. However, the detailed mechanisms still remain controversial [36-38].

Pore size is one of the most important physical parameters of a mesoporous thin film layer. Although it might be intuitive to assume the pore size would affect the liquid diffusivity, the real situation is actually more complicated. There has not been detailed direct investigation of the dependence of ion diffusivity on the pore size of the porous matrix in the context of dye-sensitized solar cells. Moreover, conflicting observations have been reported in many dissimilar systems [39, 40]. In this thesis, my research work will be focusing on the effect of variation in the average pore diameters of the mesoporous TiO_2 thin film on the diffusivity of triiodide ions in the standard DSSC design, and thus on the overall mass transfer limited current of the device.

1.5 THESIS OVERVIEW

This thesis contains five chapters. Chapter 1 provided a brief background introduction on the major concepts involved in this study, including the basics of solar cells, structure and working physics of dye-sensitized solar cells, as well as the mass transport process in dye-sensitized solar cells, which is one of the key processes in the cell operations. It is followed by the detailed literature reviews in chapter 2. An overview was given on the recent developments in dye-sensitized solar cells, which have improved the cell efficiency and stability issues. However, the bottleneck of mass transport in the electrolyte has not yet been well-resolved, mainly due to lack of thorough understanding in the diffusion mechanisms in mesoporous thin films. Previous studies of liquid diffusion in mesopores in other systems provided controversial or even conflicting results in the range in between bulk and nano-scale.

To provide better understanding of the diffusion process in mesopores in DSSCs, especially the effect of pore size variation on the ion diffusivity, experiments were designed and described in detail in Chapter 3. Results and findings of the experiments are discussed in Chapter 4. Finally, the main conclusions of this study are summarized in Chapter 5.

The research work in this thesis has been accepted for publication by the journal, Electrochimica Acta, on 28th March 2013.

2 LITERATURE REVIEW

2.1 RECENT DEVELOPMENT IN DYE-SENSITIZED SOLAR CELLS

After more than 20 years of the original publication in Nature [16], the research on dye-sensitized solar cells are still actively ongoing. More than 1700 peer-review journal articles related to dye-sensitized solar cell have been published in 2012. A review article of dye-sensitized solar cells published in 2010 [30] summarized the recent achievements and future insights in the development of dye-sensitized solar cells. There are research projects working on almost all aspects of the device, in order to further improve its performance and stability.

2.1.1 Photoanode

As discussed in section 1.2.2, after long exploration of various kinds of metal oxide semiconductors as photoanode materials, titanium dioxide, the choice from the original publication, still offers the best performance and cost-effectiveness. Efforts have been shifted to modifying the morphology of TiO_2 photoanode. It is reasonable to deduce that the random packing of TiO_2 nanoparticles in standard DSSC is not the optimal morphology. Benefitting from the development of nanotechnology, different microstructures can be easily achieved using various template techniques.

Nanotube array of TiO_2 can be produced using simple anodic aluminum oxide (AAO) template [41]. Anodic aluminum oxide is the technology for producing nanotube array of tunable size by anodizing an aluminum film in acidic solution under proper conditions [42]. Alternatively, TiO_2 nanotubes can also be obtained by direct anodization of titanium film in fluoride-based electrolytes [43, 44]. TiO_2 nanotube-based DSSC was successfully demonstrated by Shankar et al. [45]. Jennings et al. investigated the electron transport in TiO_2 nanotubes, and concluded that TiO_2 nanotubes have superior performance in terms of charge collection efficiency and electron diffusion length [46].

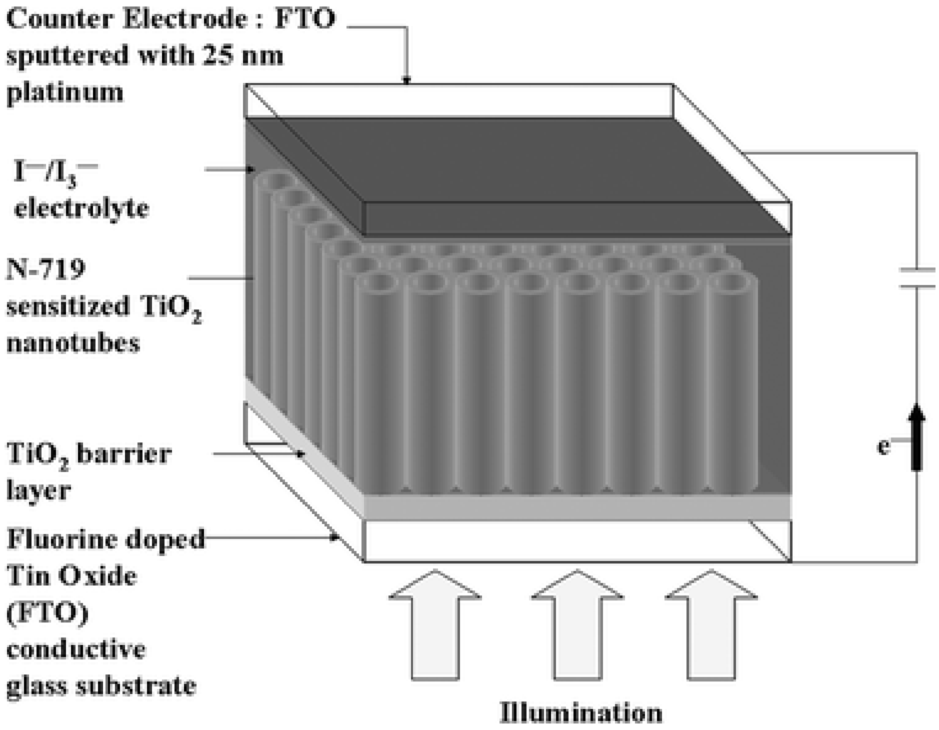

Figure 2.1: Schematic illustration of device structure of TiO2 nanotube based dye-sensitized solar cell [44]

Mesoporous TiO_2 photoanode with monodispersed pore-size was also fabricated using polymer template [47]. Self-assembly of amphiphilic block co-polymers is a powerful way to obtain ordered nanostructures [48].

However, these modifications of the morphology of the TiO_2 photoanode did not give the significant improvement we hoped for. Possible reasons may be the presence of structure defects in primitive trials, or more likely, charge injection and electron transport mechanisms, which is the subject of improvement with photoanode modification, are not the major bottleneck processes in current devices.

2.1.2 Dye Sensitizer

The most successful candidates for the sensitizer are metal-complex based dyes, represented by ruthenium complex dyes. Ruthenium based dyes have a desirable energy gap between the ground state and excited state. The positions of the energy levels are ideal for charge injection. Ruthenium dyes also exhibit excellent chemical stability after repeated oxidation and reduction reactions [30].

The recent research direction on ruthenium based dyes focused mainly on the modification of the ligands surrounding Ruthenium ions, targeting to improve the absorption in the near infrared region in the solar spectrum (**Fig.** 2.2), which is known as one of the disadvantages of ruthenium dyes. Nazeeruddin et al. [49] synthesized a Ru-based dye (N749) which has three thiocynanato ligands and one terpyridine substituted with three carboxyl groups. A red shift in the metal to ligand charge transfer band was observed. The Incident Photon to Charge Carrier Efficiency (IPCE) spectrum showed substantiated improvement of absorption by extending beyond the visible region into near-IR range up to 920 nm wavelength [50].

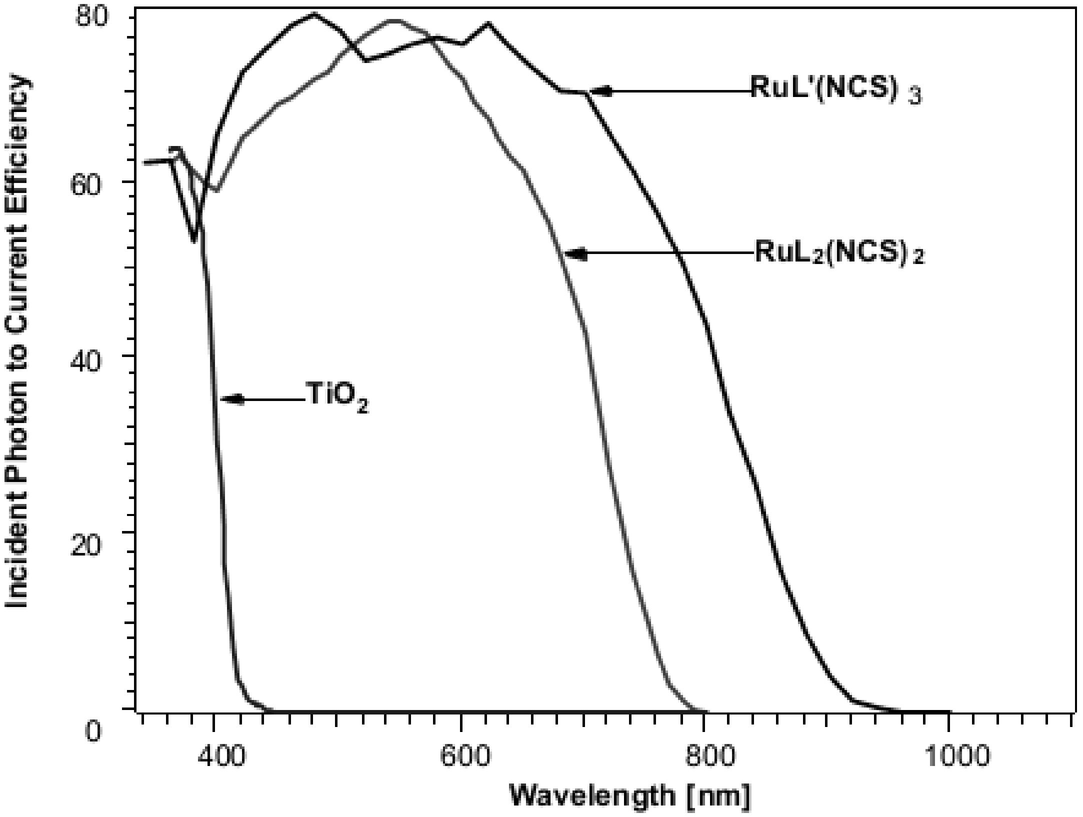

L = 4, 4'-COOH-2,2'-bipyridine
L = 4,4',4" -COOH-2,2':6',2"-terpyridine

Figure 2.2 : IPCE spectra of TiO_2 and ruthenium based dye molecules with different ligand groups [51]

It is foreseeable that the mass production of ruthenium dye will be restricted by the scarcity of ruthenium element and associated environmental issues. In addition, organic dyes have the advantages of higher extinction coefficient, which means a smaller amount of dye is required for sunlight adsorption. There are countless types of different organic dyes. Due to the nature of the organic compound, the optical and electrical properties can be easily tuned by modifying the functional groups in the molecules. Successful attempts have achieved comparable efficiency with respect to devices using ruthenium based dyes [52, 53].

2.1.3 Electrolyte

The electrolyte used in the classic design of DSSC was I^-/I_3^- redox couple in acetonitrile or other similar organic solvent. They generally have very low viscosity allowing for fast ion diffusion. In the recent years, the high volatility of organic solvent has become an issue for long term stability due to possible evaporation and leaking problems.

Replacing organic solvent by ionic liquid as electrolyte was first tested by Grätzel’s lab [54] because of its low vapor pressure and high ionic strength. The representative of ionic liquid electrolyte is the imidazolium based family. However, the high viscosity of ionic liquid severely affects the completeness of pore filling (especially in nanopores), as well as the mass transfer via ion diffusion, which becomes the bottleneck process of the device performance. Recent publications applying eutectic mixture to lower the viscosity has shown positive results [55], however the problem of slow mass transfer rate would remain under high exciton output conditions.

Quasi-solid gel electrolyte has a similar problem. By proceeding gelation process on organic solvent or ionic liquid, the liquid phase electrolyte turns into quasi-solid state [56]. Quasi-solid electrolyte is different from solid state hole conductor because the charge transport in gel electrolyte is still via ion diffusion. The evaporation and leaking problem can be solved by using quasi-solid state electrolyte. However, the diffusion coefficient of ions will be compromised, proven by the decrease of cell efficiency [57, 58].

In conclusion, the review of the recent development of dye-sensitized solar cells substantiates the paramount importance of mass transfer of ions in electrolyte in future devices. The advancement of dye sensitizer provides higher current output. This needs to be matched by enhanced electron transport in the photoanode and fast charge transfer in electrolyte. However, although with improved stability, the mass transfer rate in a novel electrolyte is actually slower than the classic design. Therefore, the bottleneck condition of mass transfer in electrolyte is expected to be more critical in the future development of DSSCs.

2.2 LIQUID DIFFUSION IN MESOPORES

The diffusion of liquid molecules in small pores have attracted intense interest in research study. As mentioned above, in the range of mesopores (2-50 nm), both bulk and microscopic effects may influence the liquid diffusion, depending on different systems of interest. There are two main opposite views from literature.

2.2.1 Pore-size Independent Diffusion

It is generally believed that the liquid diffusivity is pore size independent when λ, the ratio of molecular size to pore diameter, is greater than 0.1 [31]. Considering the sizes of most liquid molecules are in the range of a few angstroms (Å), this means the liquid diffusion should be pore-size independent for most mesoporous materials. The basis of this argument is the short mean free path of intermolecular collision. The collision of liquid molecules in porous materials consists of two different collision mechanisms, namely intermolecular collision and collision between liquid molecules and the pore wall. The overall mean free path is calculated as:

$$\frac{1}{\lambda_{total}} = \frac{1}{\lambda_{molecular}} + \frac{1}{\lambda_{pore}} \tag{2.1}$$

Since $\lambda_{molecular}$ is small compared to the molecular size, the first term in the right side of equation will be significantly larger than the second term. Therefore, the overall mean free path of collision will be little affected by the collisions on the pore wall, and results in pore-size independent diffusion [31]. In this case, the ratio of the effective diffusivity of the porous matrix (D_{Matrix}) to the bulk diffusion coefficient (D_{Bulk}) depends only on the porosity (ε) and matrix factor (q) of the material [59],

$$D_{Matrix} = D_{Bulk} \times \frac{\varepsilon}{q} \tag{2.2}$$

ε is the porosity and q is the matrix factor of the porous thin film, $q = \tau^2/\delta$, where τ is the tortuosity factor and δ is the constrictivity factor [36]. The constrictivity factor δ is a measure of the fluctuations of the effective cross-sectional areas encountered on these diffusion paths [60]. And the tortuosity factor, is a parameter describing how tortuous the porous matrix is. As illustrated in **Fig**. 2.3, the tortuosity factor is calculated as the average ratio of the length of curve path (L) to the straight line distance (C) between two points in the porous material.

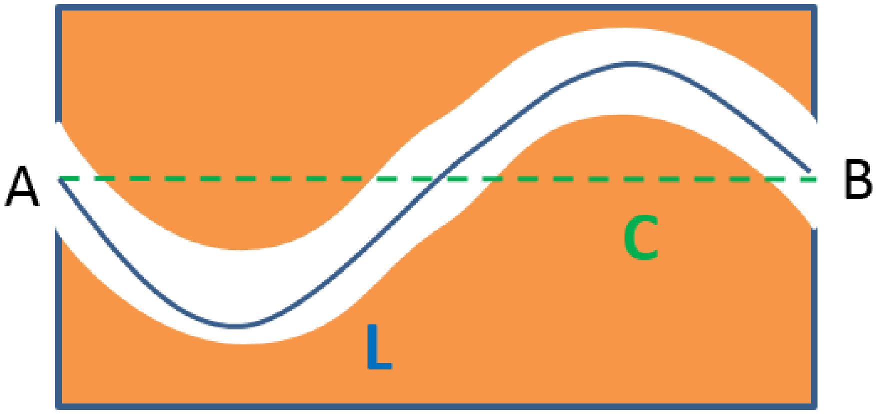

Figure 2.3: Illustration of the tortuosity factor in porous media

As the diffusion in liquid is mainly by molecular mechanism, according to the equation (2.2), the diffusivity should be independent of the pore diameter in most mesoporous materials.

2.2.2 Pore-size Dependent Diffusion

However, it is often observed in many systems, the diffusion was impeded when the λ value was much smaller than 0.1 [61, 62] . In those cases, the diffusivity of the liquid molecules heavily depends on the pore diameters of the mesopores. The decrease of diffusivity with respect to the average pore diameters is usually approximated by an exponential decrease [63, 64]. The theoretical basis of this observation is often associated with possible surface interaction and bonding mechanism between the liquid molecules and the pore wall, which decreases the effective pore volume, thus leading to significant steric hindrance effect of the pore wall.

Mitzithras et al. 1992 studied the diffusivity of liquid cyclohexane in porous silica media by Nuclear Magnetic Resonance (NMR) [61]. The diffusivity of cyclohexane was found to be affected at the pore scale of 40 nm (**Fig.** 2.4). Considering the molecular size of cyclohexane is about 5.8 Å, the diffusivity is impeded when the λ value is close to 0.015.

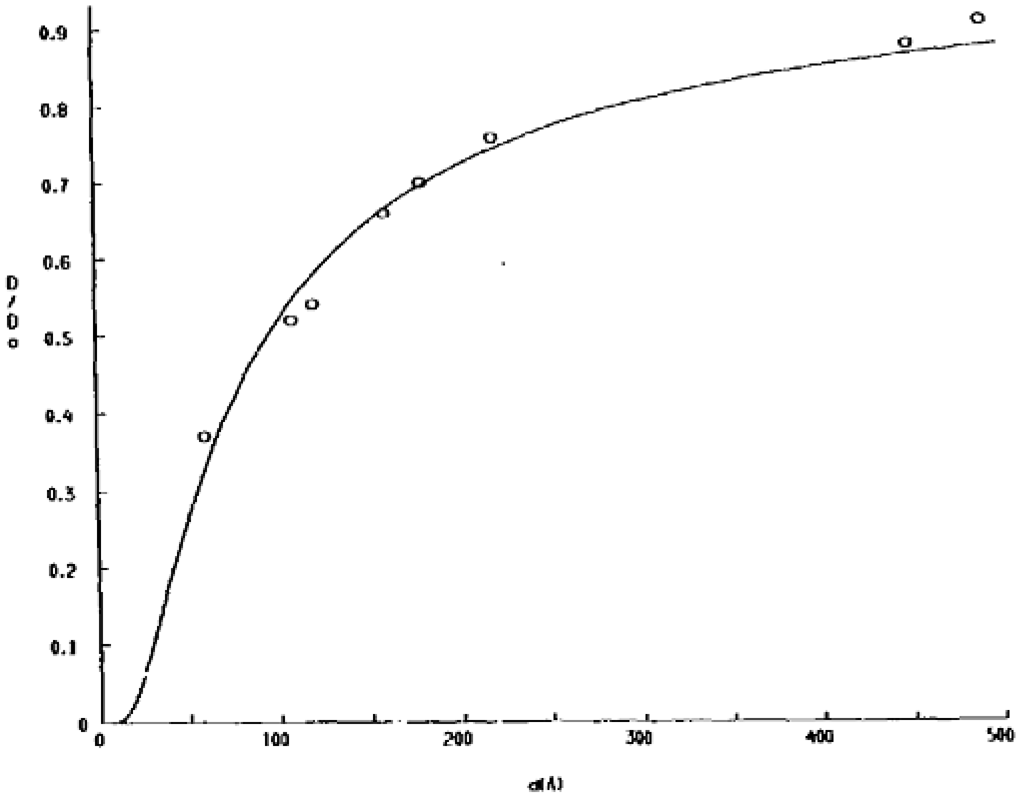

Figure 2.4: Effective diffusivity of cyclohexane with respect to the pore diameter of porous silica [61]

Koone et al. (1995) investigated the diffusion of various types of simple liquid in porous sol-gel glass [62]. He found the diffusion of various liquid molecules are hindered in 2.9 nm pores. The λ value in this case approximates 0.1 for most molecules. The extent of hindrance of different liquid molecules vary significantly even if they have similar molecular sizes. This indicates that the relationship between liquid diffusivity and pore-size is highly dependent on the system. It is interesting that the diffusion coefficients of polar liquid molecules seem to be less impeded than those non-polar molecules. This is actually counter-intuitive since polar molecules should more easily bond with the surface atoms of pore wall. The author rationalized this observation with the assumption of high mobility of adsorbed molecules on the surface.

2.2.3 Previous Studies in Dye-sensitized Solar Cells

There have been a number of interesting studies on ion diffusion in dye-sensitized solar cells. Yun et al. (2011) investigated the effect of changing pore-size to the overall performance of the DSSC [65]. They found that the sample with small pores and pore volume have lower quantum efficiency and thus poorer performance. However, it is unquestionable that the overall performance of a device is a complicated outcome. It depends on many parameters. Therefore, from my point of view, it is more advisable to separate the effects of pore-size change on different aspects, such as dye loading, light harvesting, mass transport, charge transport, etc. Chen et al. (2011) performed a similar study in quasi-solid dye-sensitized solar cells [66]. The variation of pore size was achieved by stacking TiO_2 microspheres of different diameters. Since the TiO_2 spheres used exhibit relatively large sizes, the main factor affecting the performance is the light scattering due to the photoanode.

Yang et al. (2011) studied the effect of pore structure on the mass transport rate of ions in the electrolyte [38]. A comparison is made between porous film with bi-modal and uni-modal size distribution, on the mass transfer limited current and the open circuit voltage (V_{oc}). According to his finding, the bimodal size distribution would lead to higher V_{oc} and faster mass transport rate of ions. Similar studies on the mass transport rate in solid-state devices from different aspects were carried out [67, 68].

However, there is a lack of detailed study on the direct relationship between ion diffusivity and pore-size of the mesoporous TiO_2 film. With two conflicting views regarding liquid diffusion in mesopores mentioned above, the critical question remains in dye-sensitized solar cells, whether the ion diffusivity is indeed pore-size independent in the mesopores of photoanode. Furthermore, it is well known that some essential fabrication processes of DSSCs, such as dye-loading and $TiCl_4$ post-treatments, will lead to the shrinkage of pore diameters [69, 70]. It is crucial to understand the influence of these processes to the mass transport rate, and thus to the overall cell performance.

2.3 MEASUREMENT OF ION DIFFUSIVITY

The conventional methods to measure the diffusivity of liquid molecules include NMR, radioactive tracer diffusion, thermal neutron scattering and light scattering [31]. Ion diffusion in liquid electrolyte is focused in this thesis. Since these ions are charged, it is much easier and also more accurate to measure the diffusivity using electrochemical measurements. The most common and available electrochemical measurement methods are Electrochemical Impedance Spectroscopy (EIS) and direct current (DC) polarization measurement. Both are designed for the measurement of thin layer cells [37].

2.3.1 Electrochemical Impedance Spectroscopy

Electrochemical Impedance Spectroscopy is a powerful tool in electrochemical analysis. It measures the current response of the system under alternating current (AC) perturbations of variable frequencies. It is able to reveal most of the charge transport and transfer process taking place under operating conditions. The data analysis of EIS usually requires appropriate modelling and construction of an equivalent circuit of the system. It has proven to be extremely useful in the studies of porous electrode/electrolyte interaction. For example, Bisquert et al. [71-73] performed detailed studies on the interaction between the transporting electrons in the electrode and the ions in the electrolyte using sophisticated impedance techniques. Phadke et al. [74] used EIS to analyze the charge transfer mechanism at the porous electrode/electrolyte interface.

The ion diffusion impedance within a thin layer cell with only electrolyte between two electrodes can be well described by the Nernst Diffusion element Z_N [37, 75]. The impedance Z_N can be expressed as

$$Z_N = \frac{Z_0}{(i\omega)^{0.5}} tanh(i\tau_d\omega)^{0.5} \tag{2.3}$$

where ω is the angular frequency, Z_0 and τ_d are the Warburg parameter and characteristic diffusion time constant. Those are the two key parameters both related to the diffusion coefficient of the ions, in the ways expressed in the following equations,

$$Z_0 = \frac{RT}{n^2F^2c_0A\sqrt{D}} \tag{2.4}$$

$$\tau_d = \delta^2/D \tag{2.5}$$

where R is the molar gas constant; T is temperature; n is the stoichiometry constant which equals 2 for iodide/triiode redox couple; F is the Faraday constant; c_0 is the molar concentration of triiodide ions; A is the cell area; δ is the thickness of diffusion layer; D is the bulk diffusion coefficient of triiodide ions. Due to the symmetry of the thin layer cell, the thickness of the diffusion layer can be determined as δ = d/2, where d is the distance between electrodes [76]. The Nernst diffusion impedance appears at the lower frequency of the impedance spectroscopy. It typically shows a straight line at higher frequency and a semicircle at lower frequency. By data fitting with a finite length Warburg element, the value of diffusion coefficient can be determined.

The equivalent circuit of a simple device containing only electrolyte between electrodes is straightforward, shown in **Fig.** 2.5. R_s represents the series resistance of the device, originated from the resistance of wire, connection, and the surface resistance of FTO glass. R_{CT} is the charge transfer resistance at the electrodes. The magnitude of R_{CT} is in the range of a few ohms with platinum catalyst. The charge transfer capacitance at the electrode/electrolyte interface results in the constant phase element (CPE). A CPE is used for data fitting because the surface roughness of the FTO/Pt electrodes after Pt coating modifies the behavior from ideal capacitance [75]. Z_N is the Nernst diffusion element which can be treated as a finite length Warburg element for data fitting.

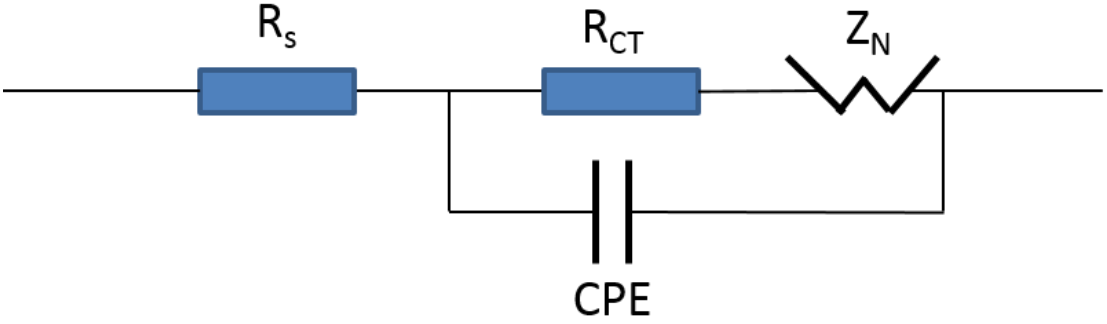

Figure 2.5: Equivalent circuit of a thin layer device with only electrolyte between electrodes

However, in the case of dye-sensitized solar cells with the presence of mesoporous TiO_2 thin film, the situation is much more complicated. The device is no longer symmetrical and there are two dissimilar diffusion layers (bulk diffusion and diffusion in porous film) connected in series. The equivalent circuit of multi-layer diffusion is analyzed by Freger [77], which involves various assumptions and complicated model construction. Accurate information of ion diffusion in mesoporous film is difficult to isolate from the overall impedance spectrum due to the interference from bulk diffusion layer.

Another problem of using impedance for the analysis of ion diffusion is the low resonance frequency, resulting in a large time constant and thus prolonged duration of measurement. This could lead to less reliable results in this particular case due to the possible cell degradation and the electrolyte evaporation.

2.3.2 DC Polarization Measurement

DC polarization measurement is more frequently used in the previous studies in DSSCs related to ion diffusion [36, 70]. The Pt-coated FTO electrodes exhibit minimal charge transfer resistance (≈2 ohms) [37], and hence the redox reaction happening under polarization is diffusion controlled. The concentration of diffusion species (triiodide ions) is shown in **Fig.** 2.6. In thin layer cells used in this thesis, the diffusion layer thickness is equal to the distance between electrodes [76].

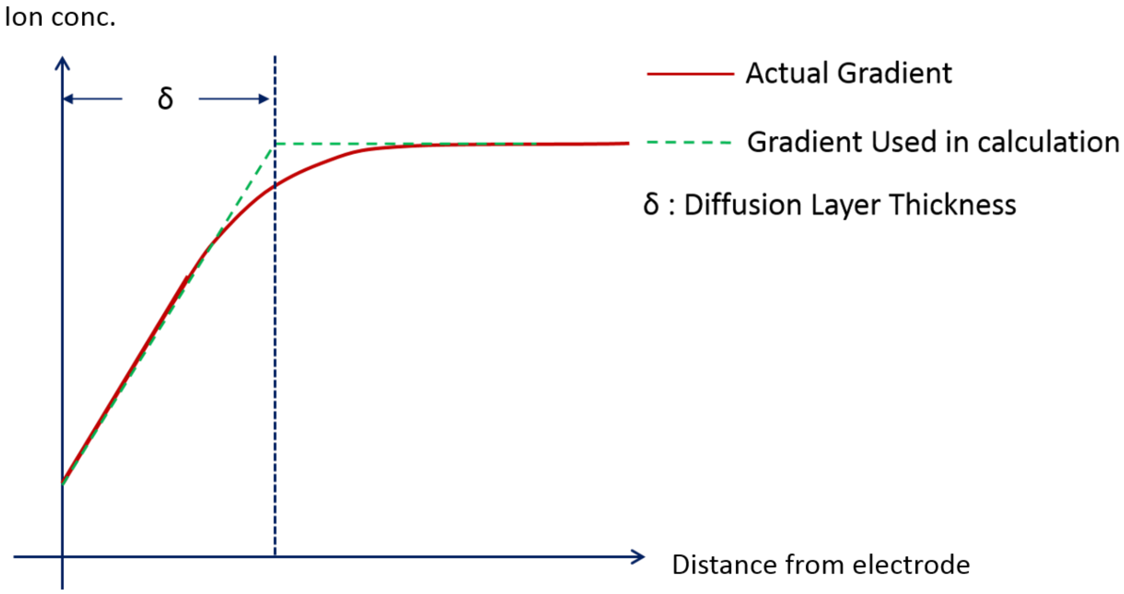

Figure 2.6: Triiodide ion concentration profile under DC polarization condition

The current density under over-potential can be calculated from the ion flux **Eq.** 1. 2. With the assumption of a linear concentration gradient due to constant current density throughout the device, the current density in the electrolyte between two electrodes can be further simplified to:

$$J_{lim} = \frac{2nFcD}{d} \tag{2.6}$$

where c is the bulk concentration of triiodide ions in the electrolyte.

With the presence of a mesoporous TiO_2 thin film within the cell, construction of an appropriate mathematical model is required to determine the diffusion coefficient of triiodide in the mesoporous layer. In the previous studies conducted by Kron et al. [36]

and Papageorgiou et al. [70], slightly different models were constructed to calculate the diffusion coefficient of triiodide ions. In Papgeorgiou's model, the diffusion coefficient of triiodide ions in a porous matrix is assumed to be the bulk diffusion coefficient (D_{bulk}) multiplied by the porosity, which is not entirely accurate. In this study, the model proposed by Kron is used.

Because the device is unsymmetrical, the limiting current density values depend on the direction of current flow [70]. Forward bias was used in this study, consistent the potential of the TiO_2 thin film under operating conditions. Under limiting current density condition, the concentration profile of triiodide ions in the device is estimated and shown in **Fig.** 2.7

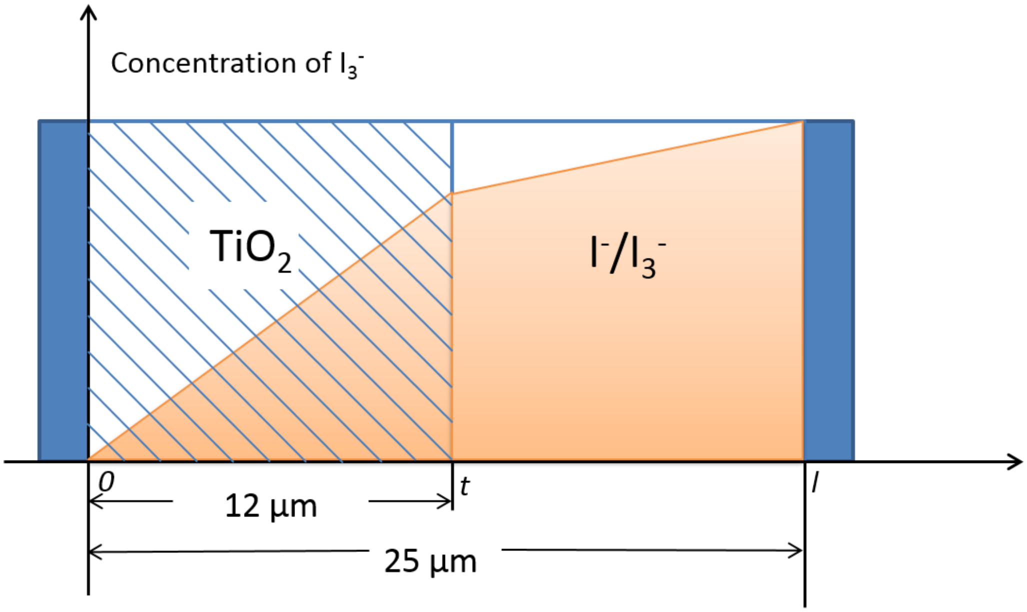

Figure 2.7: Triiodide ion concentration profile in a dye-sensitized solar cell under limiting current condition (forward bias)

Considering the continuity of current throughout the device, the current density in the TiO_2 porous film should be equal to the current density in bulk electrolyte:

$$J_{lim} = 2FD_{TiO_2}\frac{c^t - c^0}{t} = 2FD_{bulk}\frac{c^l - c^t}{l-t} \tag{2.7}$$

where D_{TiO2} and D_{Bulk} are the effective diffusion coefficients in porous film and bulk electrolyte respectively. c^l, c^t, c^0 are the local concentration of triiodide ions at position l, t, 0 respectively. Furthermore, the conservation of mass of triiodide ions in the device gives the following expression:

$$c[\varepsilon t + (l - t)] = \varepsilon\frac{c^t + c^0}{2}t + \frac{c^t + c^l}{2}(l - t) \tag{2.8}$$

where ε is the porosity of the mesoporous film. Combining (2.7) and (2.8) with appropriate boundary condition at limiting current, $c^0 = 0$, the final expression of limiting current can be obtained as follows,

$$J_{lim} = 4Fc\frac{D_{TiO_2}D_{bulk}(\varepsilon t - t + l)}{D_{TiO_2}(l-t)^2 + D_{bulk}(\varepsilon t - 2t + 2l)} \tag{2.9}$$

Therefore, from limiting current values, the effective diffusion coefficient in mesoporous TiO_2 can be calculated from **Eq.** 2.9. The values of other parameters, including bulk diffusion coefficient, film thickness and porosity, need to be determined before the calculation.

3 EXPERIMENTAL

3.1 DEVICE FABRICATION

Most of the procedures used here to manufacture a dye-sensitized solar cell device were similar to the standard procedures in the literature [78]. Since only ion diffusivity was concerned in this study, the sample devices were not working cells but a modified version of classic dye-sensitized solar cell design. The main differences were the following: the TiO_2 thin films were not loaded with dye molecules, and both electrodes were coated with platinum which acts as catalyst for the redox reaction in the electrolyte. All the measurements were conducted in dark to prevent any photon-excitation. Therefore, the TiO_2 mesoporous thin film during the measurements were mostly electro-inactive and acted as physical barrier of diffusion, for the purpose of investigating the ion diffusion behavior in mesopores.

3.1.1 Titanium Dioxide Paste Preparation

The mesoporous TiO_2 thin film is made from random stacking of TiO_2 nanoparticles. The most common deposition method is a solution process of TiO_2 paste followed by heat treatment [79]. It is also the method used in this study. The procedures of making TiO_2 paste is similar to those in the literatures [78], with slight modifications. The detailed steps are as follows:

1. 0.25 g P25 TiO_2 nanoparticles (99.5% Sigma Aldrich, 75% anatase) were weighed and added to a mortar.
2. 0.4 ml of acetylacetone ($\geq$ 99%, Sigma Aldrich) was added to the mortar, followed by grinding for a few minutes until a uniform mixture was obtained.
3. 0.8 ml of de-ionized water was slowly added into the mortar in 2 minutes, with constant grinding
4. 6.5 ml of anhydrous ethanol was slowly added into the mortar in 5 minutes, with more vigorous grinding. A white color dilute suspension was produced.
5. 0.83 g of α-terpineol (96%, Alfa Aesar) was added into the suspension. Terpineol is the key ingredient which promotes the formation of mesoporous structure, by keeping the nanostructure from collapsing at the beginning of the sintering process.
6. 1.25g ethyl-cellulose ethanol solution (1:9 weight ratio) was added into the mixture. Ethyl-cellulose can effectively reduce the chance of cracking in the porous thin film.
7. The mixture was ground and dried at the same time, in order to evaporate the excess de-ionized water and ethanol. The final product should be white viscous paste with minimal amount of ethanol and water in it.

Now with the TiO_2 paste ready, the mesoporous films can be easily manufactured by the simple screen printing process. The quality of the TiO_2 paste is directly related to the quality of the final mesoporous thin film.

3.1.2 Device Assembly

In order to focus on the ion diffusivity in the mesoporous thin film, a modified version of dye-sensitized solar cells was fabricated, with the following procedure,

1. Two pieces of FTO glass (2.5cm × 1.5cm) were prepared. A small opening (≈ 1 mm^2) was drilled in one piece of glass using a diamond drill.
2. The two pieces of FTO glass were cleaned step by step in detergent solution (Hallmanex II), deionized water, acetone and Isopropyl alcohol by ultra-sonication for 15 minutes in each step.
3. Platinum catalyst layer was deposited on each FTO glass by heat treatment of chloroplatinic acid (H_2PtCl_6). In this step, one drop of dilute H_2PtCl_6 solution in anhydrous ethanol (C_2H_5OH) was dipped onto the conductive surface of each FTO glass. The two pieces of FTO glass were subsequently heated to 400°C for 15 minutes.
4. TiO_2 mesoporous thin film was deposited onto the intact FTO glass by screen printing process, which is illustrated by the drawing in **Fig.** 3.1. A uniform thin film can be easily made from this procedure. The shape of the film depends on the shape of the aperture while the thickness is determined by the thickness of the screen printing membrane.

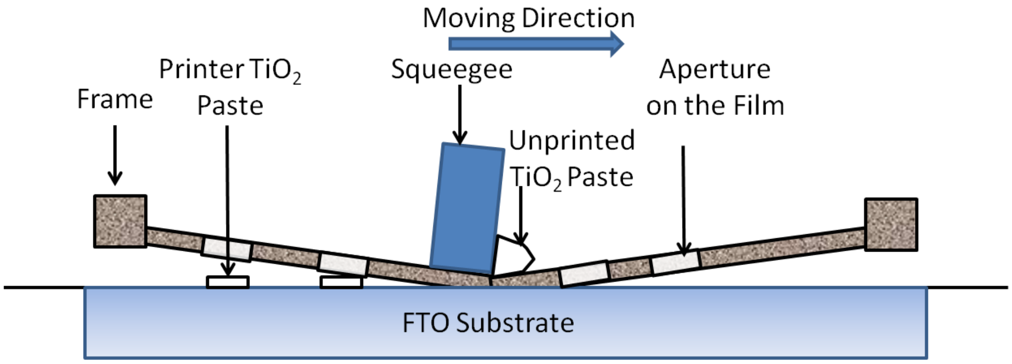

Figure 3.1: Schematic illustration of the screen printing process [19]

5. The FTO glass with film paste would be heated up to 450°C for 15 minutes followed by 500°C for another 15 minutes. The heating and cooling rate should be kept low (<15°C/min) to avoid possible cracking of the film. The resultant mesoporous TiO_2 thin film may undergo additional $TiCl_4$ treatments before proceeding to next step. The $TiCl_4$ treatments were primarily for pore-size variation purpose, which will be described in detail in Section 3.1.4.
6. The two pieces of FTO glass, one with TiO_2 film and one with the opening, were then sealed together using Surlyn film (Meltonix 1170-25, Solaronix). The thickness of the surlyn film is 25 μm. It will automatically soften and adhere to the FTO glasses in the oven at 100°C for 1 minute.
7. Electrolyte was then injected into the space between the FTO glasses from the hole on the top, consisting of 0.03 M I_2 (Sigma Aldrich, 99.8%) and 0.3 M NaI (Sigma Aldrich, 99.5%) dissolved in acetonitrile (Sigma Aldrich, anhydrous 99.8%).

8. Finally the small opening would be sealed by a small piece of cover glass with glue. A typical structure of the device fabricated is shown in **Fig.** 3.2.

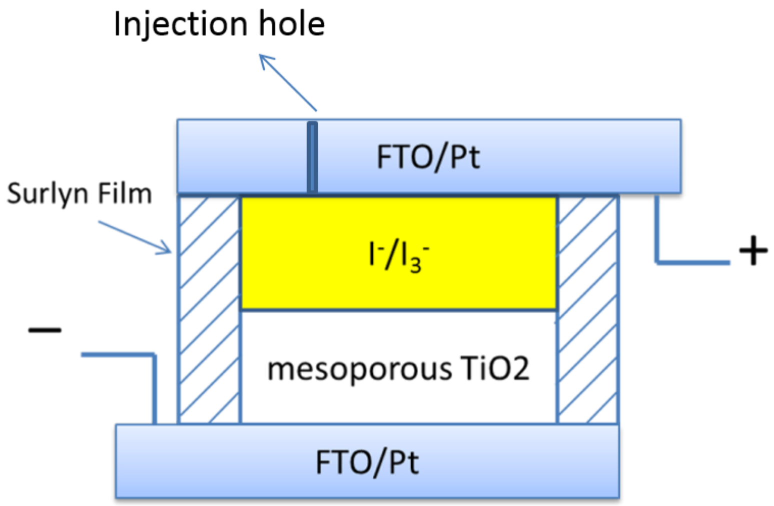

Figure 3.2: Structure of a thin film device fabricated in this study

3.1.3 Vacuum Backfilling of Electrolyte

Due to the tiny spacing between electrodes and sealed environment in the device, it is difficult to directly inject electrolyte into the space between the two electrodes. Even if the electrolyte is successfully pushed into the device, it is uncertain if the filling is complete. Complete filling of electrolyte is one of the assumptions in the calculation of triiodide ion diffusivity from **Eq.** 2.9.

The technique of vacuum backfilling was applied to ensure better electrolyte filling of the sample devices. As the name implies, it utilizes ambient pressure to push the electrolyte into the device. It was applied after the sealing procedure, with the following steps:

1. The surface of the FTO glass with the small opening on it, was cleaned by de-ionized water and acetone.
2. The sample device was placed in a glass container, with the small opening facing upwards.
3. A small tip containing electrolyte was placed at the opening of the FTO glass.
4. The glass container was then swiftly closed up. The mechanical vacuum pump connecting to the glass container was subsequently turned on.
5. While the air in the glass container evacuated from the glass container, air bubbles would appear in the electrolyte. This is an indication of air coming out from the space between the electrodes in the device.
6. After a few seconds, when there was no more bubbles coming out from the device, the vacuum pump was turned off. Air was slowly introduced back into the container. The pressure of the air would push the electrolyte into the device from the small opening.
7. The tip of electrolyte was then removed from the opening. The device was sealed with a piece cover glass.

The drawing of the setup of a vacuum backfilling system is shown in **Fig.** 3.3. It is a simple yet effective technique for electrolyte filling process. One challenge is the low vapor pressure of acetonitrile. Therefore the whole procedure needs to be completed fast to prevent excessive loss of solvent in vacuum environment.

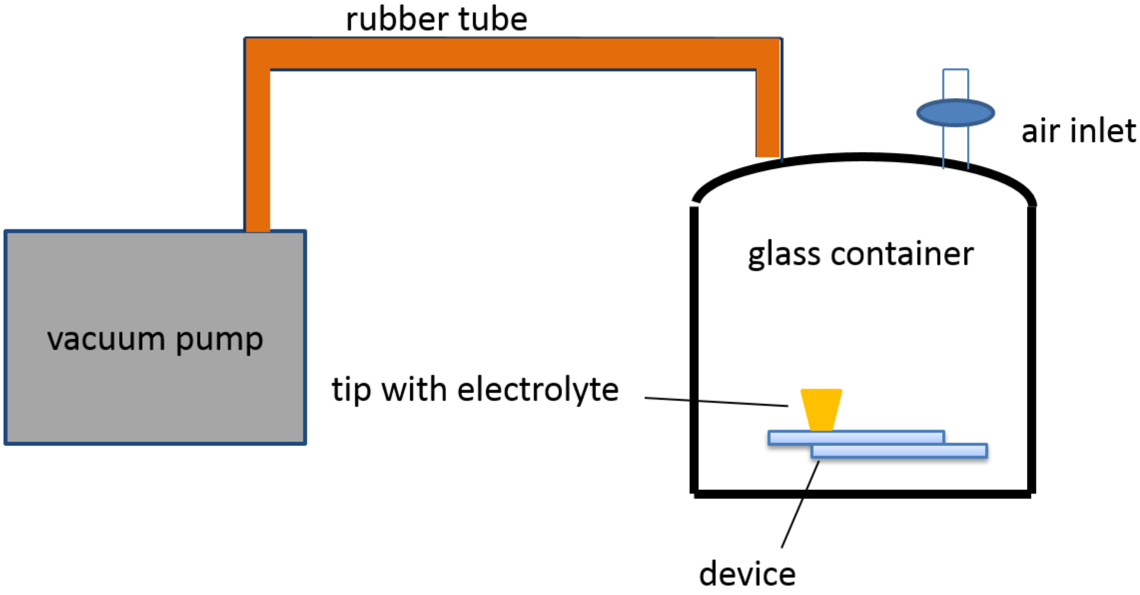

Figure 3.3: Schematic drawing of the set-up of vacuum backfilling

3.1.4 Titanium Tetrachloride Post-Treatment

Titanium tetrachloride post-treatment is widely used in dye-sensitized solar cell fabrication. It is proven to be beneficial to the overall cell performance by reducing recombination rate, and improving the charge injection efficiency from excited dye molecules to the conduction band of TiO_2 [80, 81]. The basic mechanism of $TiCl_4$ post-treatment is a chemical bath reaction which forms a layer of TiO_2 (anatase) on top of the surface of the original TiO_2 mesoporous thin film by epitaxial growth [69]. Therefore, $TiCl_4$ treatments are used in this study for the purpose of pore variation. Due to the nature of uniform epitaxial growth in the treatment, it is valid to assume that the matrix factor of the mesoporous layer, which is mostly related to the geometrical properties of the pores, would not vary significantly after $TiCl_4$ treatments [36].

Titanium tetrachloride is a colorless liquid compound. It reacts vigorously with water at room temperature, forming titanium dioxide and hydrogen chloride. It is able to react with the water vapor in air. Therefore, large amount of white fume containing TiO_2 and HCl droplets will be evolved upon exposing the $TiCl_4$ liquid to the air. All the solution preparation steps must be done in the fume hood. The $TiCl_4$ treatments conducted were similar to procedures in the literature [28], which consisted of the following steps:

1. 1.1 ml of $TiCl_4$ (99%, Sigma Aldrich) was added into 25 ml 0^oC water in ice/water bath, to form 0.1 M $TiCl_4$ aqueous solution. The low temperature is to avoid spontaneous hydrolysis reaction of $TiCl_4$ before dissolution.
2. The solution was then slowly heated up to 70^oC.
3. The FTO glass with TiO_2 thin film was immersed into the solution, held for 30 minutes
4. The thin film was taken out and rinsed with de-ionized water.
5. The sample was heated at 450^oC for 30 minutes.

After these five steps, $TiCl_4$ treated TiO_2 thin film with smaller pore-size could be obtained. These steps are considered as one $TiCl_4$ treatment, some samples needed to undergo multiple $TiCl_4$ treatments to achieve desirable pore-size variation. The procedures of $TiCl_4$ treatment and the chemical reaction involved are shown in **Fig.** 3.4.

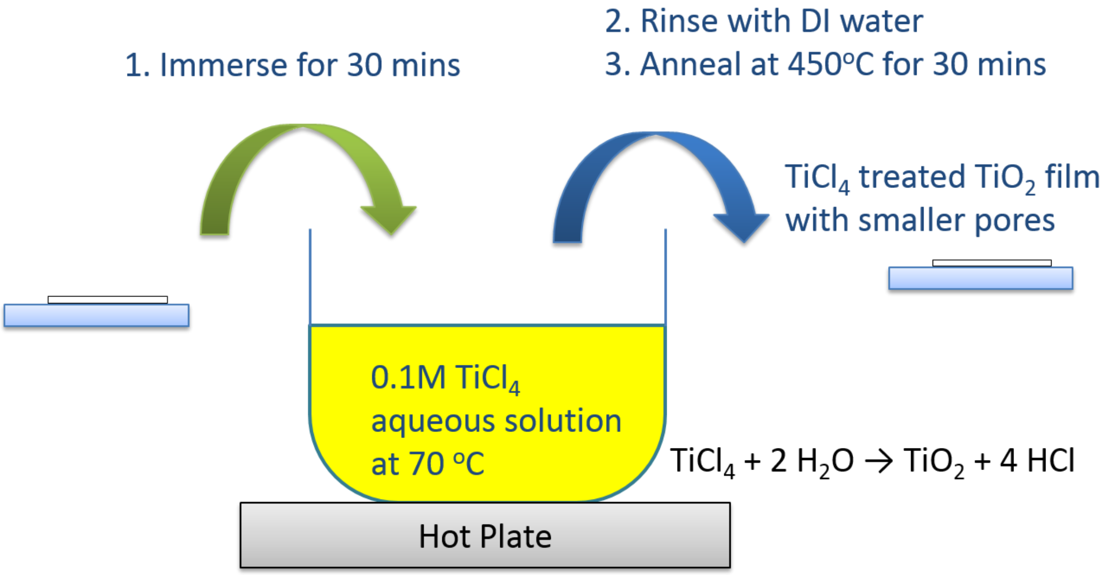

Figure 3.4: Illustration of procedures of a TiCl4 post-treatment

3.2 DEVICE CHARACTERIZATIONS

Physical, optical and electrochemical characterization techniques were conducted in order to obtain comprehensive information of the mesoporous structures and ion diffusion in these structures. The techniques of characterization used in this study will be introduced in detail in the section.

3.2.1 Nitrogen Isotherm

After variable times of $TiCl_4$ post-treatments, the variation of pore-size and porosity needs to be measured and quantified. Nitrogen isotherm (QuantaChrome Nova 2000 surface area/pore size analyzer) is an effective characterization technique to retrieve information on pore-size distribution and porosity. The simplified structure of the equipment is shown in **Fig.** 3.5. The experimental procedures are stated as follows,

1. 10 pieces of clean cover glass were weighted to get mass m_1. 10 pieces were used to ensure sufficient number of samples for reliable results.
2. TiO_2 thin film was deposited onto these glass pieces following the steps in section 3.2,
3. Desired times of $TiCl_4$ post-treatments were performed on these samples following the steps in section 3.1.4.
4. The total mass was weighed as m_2, so the mass of TiO_2 thin film would be ($m_2 – m_1$).
5. The cover glass was carefully cut into small pieces so that they could fit into the glass tube for nitrogen isotherm characterization. Only the pieces with TiO_2 film on them

would be placed into the glass tube. It is important to keep the TiO_2 films as intact as possible.

6. The resultant pore information would be based on the total weight of the samples in the glass tube. It is necessary to normalize the data to the real sample weight ($m_2 - m_1$).

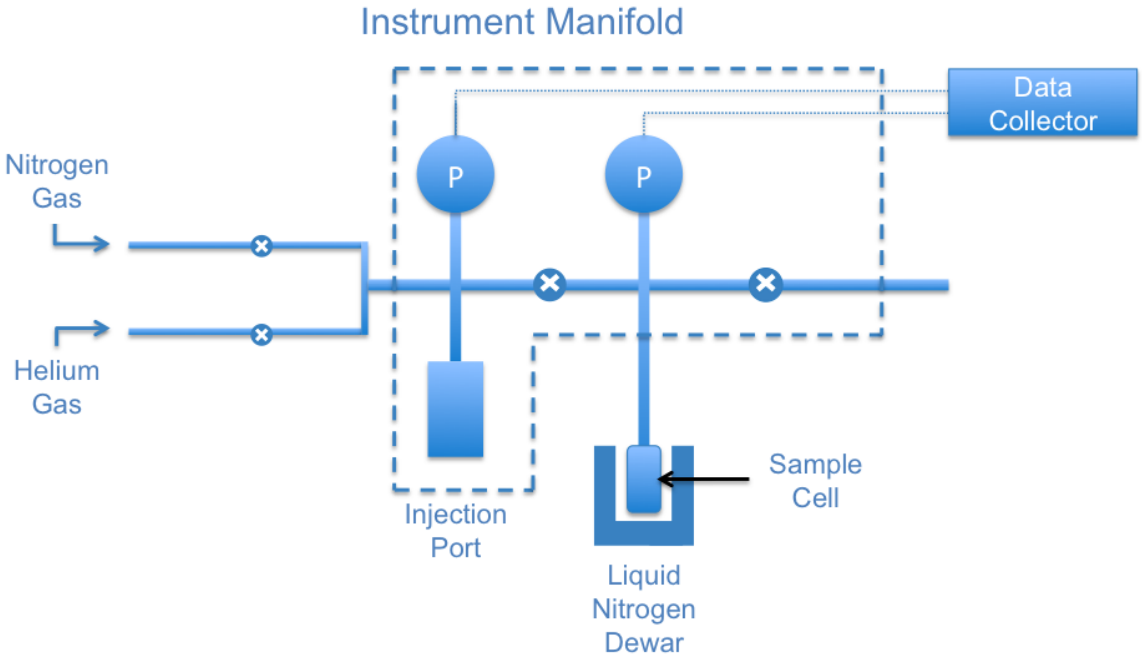

Figure 3.5: Simplified structure of a nitrogen isotherm characterization equipment [82]

Nitrogen gas is ideal for the isotherm test mainly because of its ready availability of high purity form. It also interacts strongly with most solids. Before the tests, the samples needed to be degassed overnight under vacuum at high temperature (≈200°C), in order to remove any residual adsorbed gas molecules. During the characterization process, the sample was cooled to -196°C by immersing in liquid nitrogen. This is to minimize thermal vibration, so that the amount of adsorbed nitrogen molecules could be detected. A known amount of nitrogen gas, measured by nitrogen partial pressure, is released into the sample chamber. A highly sensitive pressure transducer is used to monitor trace amounts of pressure change, in order to obtain the amount of adsorption as a function of pressure [83].

A lot of information can be extracted from the raw data of the nitrogen adsorption/desorption isotherm using different models. The Brunauer-Emmett-Teller (BET) method gives the total surface area of the samples which is less relevant in this study [84]. The Barrett-Joyner-Halenda (BJH) method provides information on pore volume distribution and hence the average pore diameter. It is a modified version of the Kelvin equation, which predicts that the gas condensation pressure in a cylindrical pore is dependent on the pore diameter. This is due to the varying curvatures at the liquid/gas interface in pores of different sizes. The BJH method extended the application of the Kelvin equation to mesopores with relatively wide pore size distribution. The derivation of the BJH method was also based on cylindrical pores, but it has been proven to be reasonably accurate in most pore structures [85]. Only pores less than 50 nm will be taken into consideration in the calculation, which is suitable for this study because smaller pores obviously play a more important role in affecting ion diffusivity.

3.2.2 Scanning Electron Microscopy

A high Resolution Scanning Electron Microscope (SEM, JEOL 7000F, Canadian Centre for Electron Microscopy) was used to observe the surface features of TiO_2 mesoporous thin film. The SEM sample preparation steps are listed below,

1. The FTO glass with TiO_2 thin film was attached onto a specimen stub using conductive carbon tape. Gloves needed to be worn at all times, to avoid possible contamination to the SEM vacuum chamber.
2. Silver paste was applied between the edges of the TiO_2 thin film and the metal stub. This was to create a path of electron flow and prevent accumulation of static charge on the sample surface.
3. The specimen would stay overnight for the silver paste to dry completely before being put into the SEM vacuum chamber for characterization.

A Transmission Electron Microscope (TEM) would generally give better image quality and higher resolution. However, extremely thin films are required for TEM characterization. Sample preparation of TiO_2 thin film is very difficult because these films are very brittle and fragile. Non-ideal sample preparation of TEM specimens would greatly compromise the image quality.

3.2.3 DC Polarization Measurement

Due to the limitations of Electrochemical Impedance Spectroscopy in analyzing multi-layer diffusion, DC polarization measurement is the major electrochemical technique used in this thesis. In a typical DC polarization measurement, the sample device was connected to programming-controlled digital multimeters (HP3478A, Electrolab Inc.) and an external DC power source. The measurements were conducted in dark to avoid possible photon-excitation in the device. The applied potential difference scanned from 0 to 1.75 V at a scan rate of 50 mV s^{-1}. Slow scan rate is important to reach steady-state condition, and to minimize possible capacitive current [76]. The resultant I-V characteristic curves were monitored and recorded by the digital multimeters. The device connection of the measurement is shown in **Fig.** 3.6.

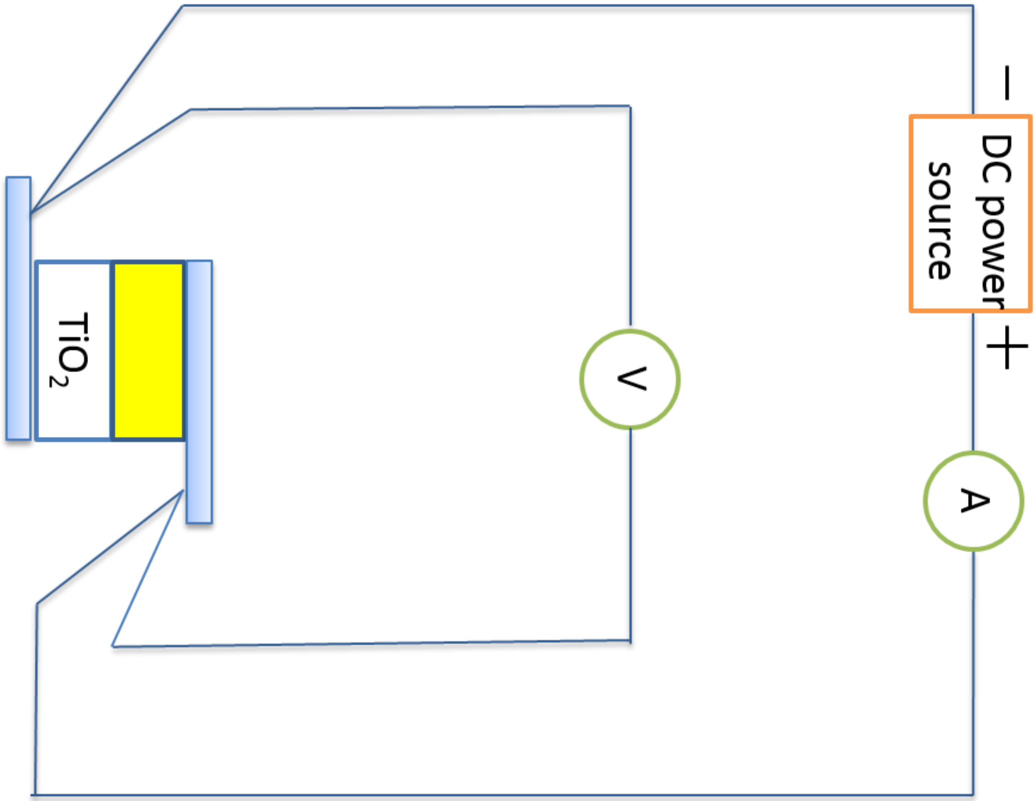

Figure 3.6: Connection of DC polarization measurement, forward biased potential difference is applied on the device

The capacitance at the TiO_2/electrolyte interface is estimated at about 500 – 1000 μF cm^{-2} [69]. The resultant capacitive current is less than 0.05 mA cm^{-2}, which is an insignificant degree of error.

3.2.4 Electrochemical Impedance Measurement

Electrochemical impedance tests were also conducted in the control samples with only electrolyte for the bulk diffusion coefficient of I_3^- ions in acetonitrile. The results were used to compare with the values obtained from DC polarization measurements to confirm its accuracy. In a typical impedance test, the sample was connected to an impedance analyzer (HP 4284A precision LCR meter) which was controlled and monitored by computer. The test frequency ranged from 1 mHz to 100 kHz. The DC input was set as zero while the oscillating amplitude was set as 25 mV, in order to maintain the linearity of the signal response.

4 RESULTS AND DISCUSSION

4.1 VARIATION OF PORE-SIZE AND POROSITY

Different samples with variable numbers of $TiCl_4$ treatments were prepared, and the change in the pore-size of the films was characterized by nitrogen isotherm. The porosity values were calculated based on the film thickness (d = 12μm, Profilometer alpha step 200), film weight and the density of anatase TiO_2. The porosity values obtained by nitrogen isotherm is less reliable because the measurements of large pores (>50nm) by BJH method are not accurate [85].

Table 4.1: The variation of average pore diameters and porosity after $TiCl_4$ treatments

Sample	Number of $TiCl_4$ treatments	Average pore diameter /nm	Porosity ε
A	0	20.91 ±1.83	0.616 ±0.018
B	1	16.92 ±2.32	0.497 ±0.010
C	2	11.33 ±2.57	0.404 ±0.014
D	3	7.97 ±1.7	0.339 ±0.008
E	4	5.7 ±1.35	0.287 ±0.006

The measurement results of the average pore diameter and porosity of each sample are listed in Table 4.1. From the values in the table, the average pore diameter decreased from 20.91 nm in Sample A before any $TiCl_4$ treatment, to 5.7 nm in Sample E after 4 times of $TiCl_4$ treatments. The overall porosity of the TiO_2 thin film decreased from 0.616 to 0.287. This means the pore volume only shrank to 46% of the original value when the average pore diameter decreased by 75%. This apparent discrepancy can be explained by the different measurement domain of pore-size and porosity. As mentioned in the experimental section, large pores (>50 nm) were not included in BJH measurement of pore-size. Only pores with diameter smaller than 50 nm were considered for the calculation of average pore diameter. However, macropores (>50 nm) do exist in the mesoporous TiO_2 thin film and contribute significantly to the total pore volume. They were included in the calculations of porosity, which were based on the film volume and the film weight. Assuming the epitaxial growth rate of $TiCl_4$ treatment is uniform throughout the surface of TiO_2 film, the fraction of pore volume change in macropores is much less than in mesopores. Let us compare the fraction of pore volume change in a 21 nm mesopore and a 200 nm macropore, assuming 8 nm coverage after epitaxial growth. The 21 nm mesopore would become 5 nm in diameter with a more than 98% decrease of volume. On the other hand, the pore volume of the 200 nm macropore will only decrease by less than 23%. This huge difference of pore volume change in mesopores and macropores after the same amount of epitaxial growth explains the less than expected drop of pore volume from 0.616 to 0.287 when the average pore diameter decreased from 20.91 nm to 5.7 nm.

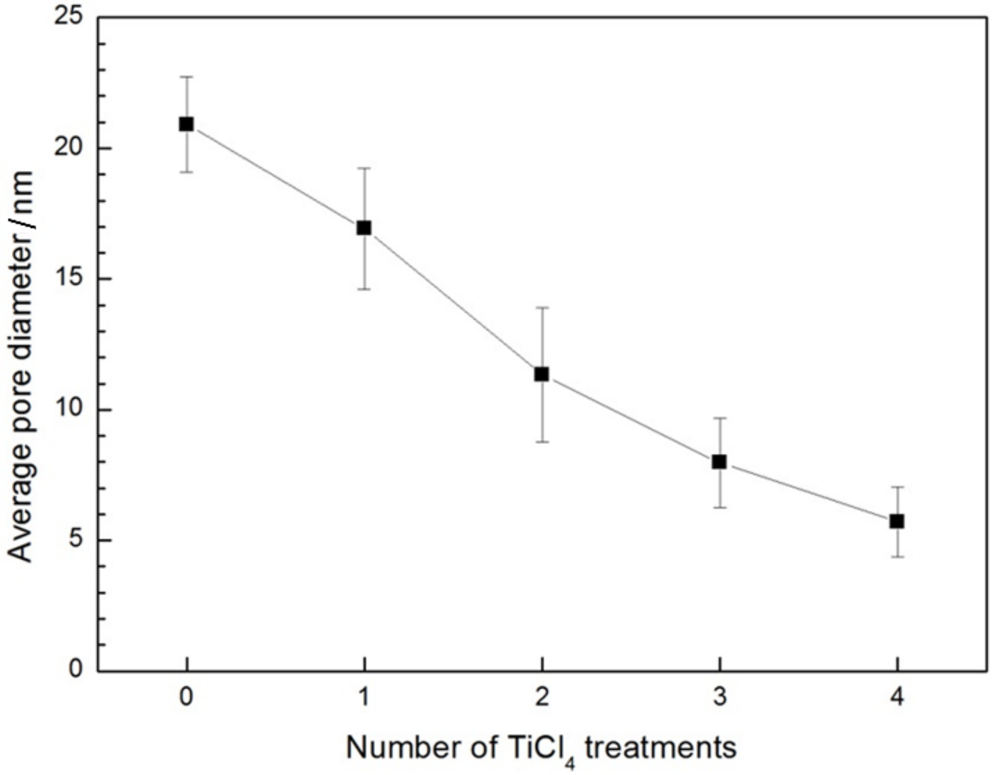

Figure 4.1: The decreasing trend of average pore diameter after different numbers of $TiCl_4$ treatments

The graph in **Fig.** 4.1 is plotted based on the data in Table 4.1. From the trend of the graph, the average pore diameter of the samples decreases almost linearly with increasing number of $TiCl_4$ treatments, which is a desirable outcome. The SEM images of sample A and sample C (after 0 and 2 $TiCl_4$ treatments) are shown in **Fig.** 4.2. Due to the small pore-size of the films and non-ideal conductivity of TiO_2, the quality of the images was not very satisfactory. However, some of the desired changes after two $TiCl_4$ treatments could still be observed. As we can see, Fig. 4.2(b) shows a denser and less porous structure than Fig. 4.2(a). This change in the surface morphology further supports the epitaxial coverage effect of $TiCl_4$ treatments.

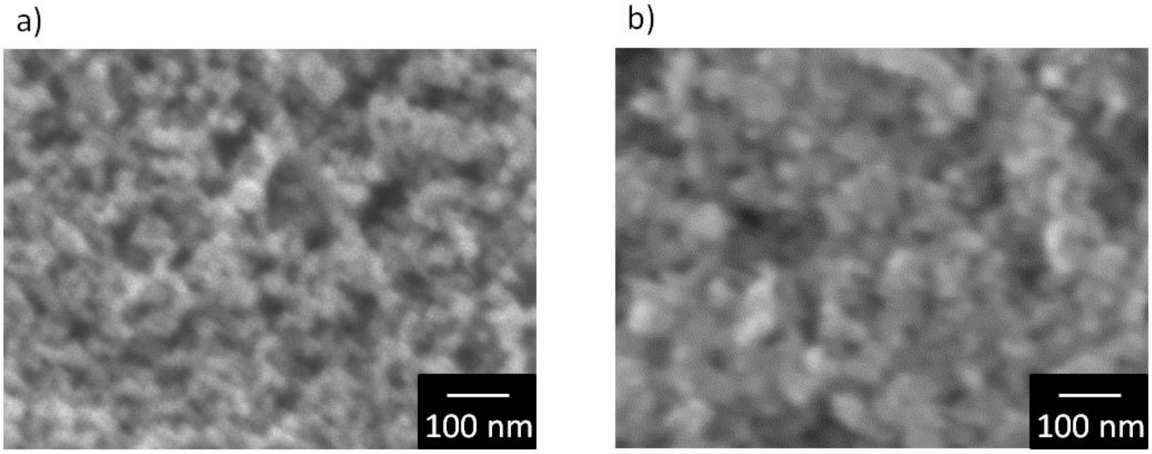

Figure 4.2: SEM images showing surface morphologies of a) Sample A before any $TiCl_4$ treatment; b) Sample C after two $TiCl_4$ treatments under the same magnification.

The typical pore-size distributions of three different samples, A, C and E corresponding to TiO_2 film after 0, 2 and 4 $TiCl_4$ treatments are shown in **Fig.** 4.3. The average pore diameter of these samples is 20.91, 11.33 and 5.7 nm respectively, as listed in Table 4.1. Due to the vast difference of the pore volumes in these three samples, the ratio percentage of differential pore volume to the total pore volume is used as y-axis of the graph, for better comparison purposes. From the shapes of the distribution curves, the pore size distributions in these samples follow more or less the normal distribution. The full width at half maximum (FWHM) values of each curve were measured as an estimate of the errors in the average pore diameters of the samples in Table 4.1, as well as the error bars in **Fig.** 4.1. The comparison of the pore-size distributions reveals that the average pore diameters decreases after $TiCl_4$ treatments while the pore-size distribution almost remains unchanged. This observation further confirms the epitaxial coverage of TiO_2 after $TiCl_4$ treatments. It is important to note that these three distribution curves were from three different samples, instead of one sample after different numbers of $TiCl_4$ treatments. This is because the samples cannot undergo further $TiCl_4$ treatments after nitrogen isotherm characterization. Therefore, it is not valid to deduce the slight variation of the distribution shapes between these samples are the consequences of $TiCl_4$ treatments.

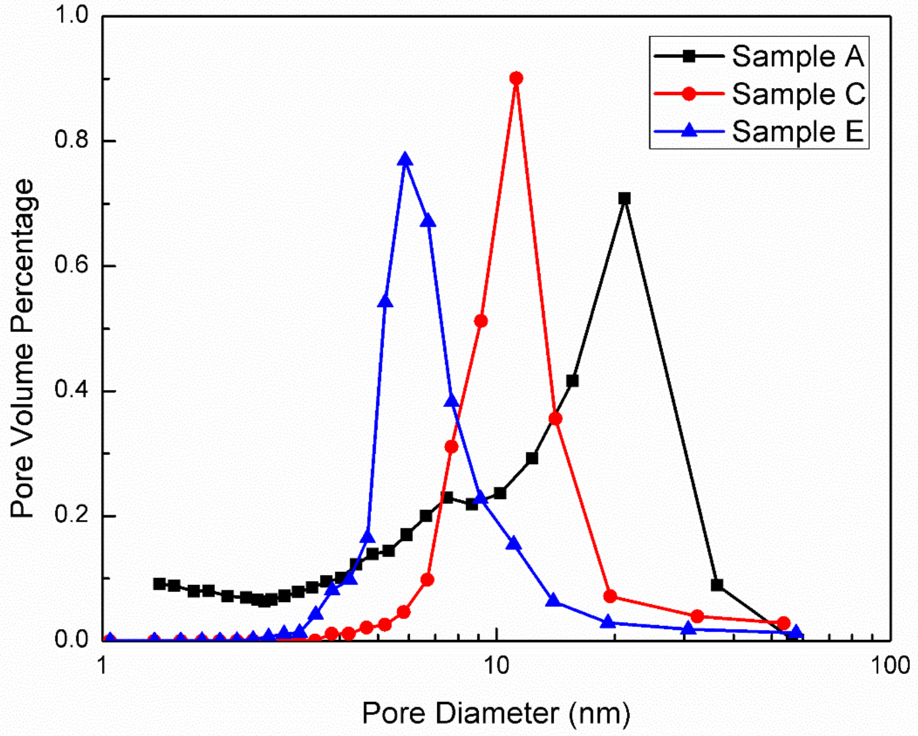

Figure 4.3: Typical pore size distributions of Sample A, C and E after 0, 2 and 4 $TiCl_4$ treatments respectively

In conclusion, the change of the pore size of TiO_2 mesoporous thin film was successfully achieved by $TiCl_4$ treatments. Based on the evidence from the change of the pore size distribution as well as the confirmation from previous studies [69], the decrease of the pore size resulted from the epitaxial coverage of TiO_2 after $TiCl_4$ treatments.

4.2 DIFFUSIVITY OF TRIIODIDE IONS

After altering the pore size of the mesoporous TiO_2 thin film, it is time to proceed to the next step of measuring the triiodide ion diffusivities in mesopores in these sample devices. Referring back to the **Eq.** 2.9, the calculation of effective diffusion coefficient in mesoporous film requires the bulk diffusion coefficient of triiodide ions.

4.2.1 Measurement of Bulk Diffusion Coefficient

The bulk diffusion coefficient of triiodide ions is determined from the control sample with only electrolyte between two FTO/Pt electrodes. Both electrochemical impedance and DC polarization methods were used to determine the bulk diffusion coefficient.

EIS

Fig. 4.4 shows the resultant Nyquist plot of electrochemical impedance of a control sample containing only electrolyte. The series resistance (≈54 Ω) is higher than expected, probably due to the particular piece of FTO glass has high surface resistance. The half circle on the left at the higher frequency represents the charge transfer process at the electrodes. The shape is distorted, possibly because of the roughness of the electrodes. This would not affect the experimental accuracy as the charge transfer process is not concerned in this study. The irregular curve on the right fit nicely to the typical shape of a finite length Warburg element.

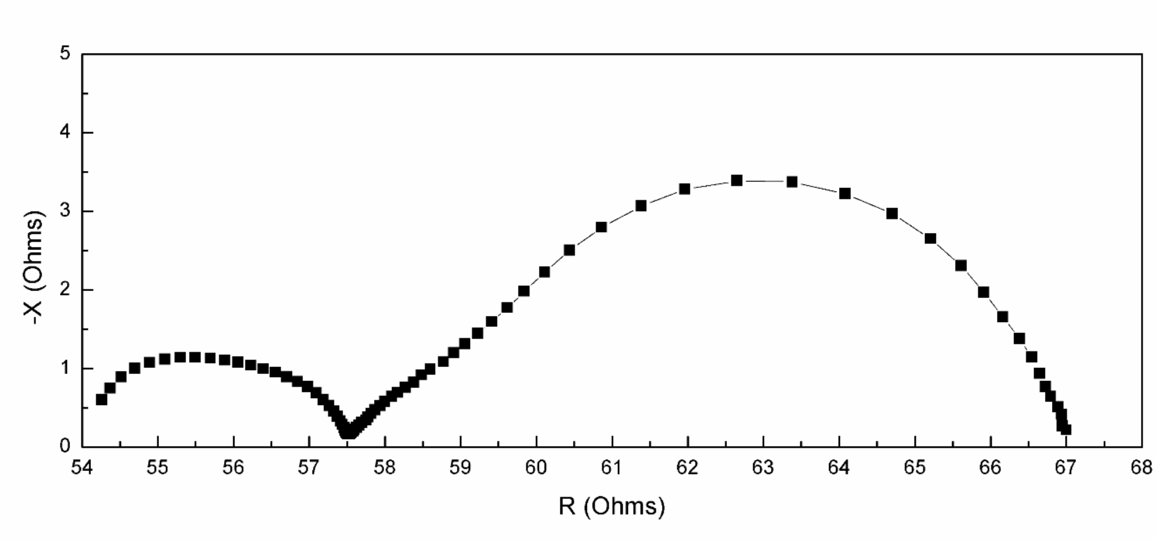

Figure 4.4: Typical electrochemical impedance spectrum of a sample device containing only electrolyte

The best fitting results gave the value of the Warburg parameter to be 1.95 s. The diffusion length in this cell was 50 μm, because a thicker spacer (100 μm) was used in the particular sample. According to **Eq.** 2.5, the bulk diffusion coefficient of I_3^- ions in acetonitrile is about 1.28×10^{-5} cm^2 s^{-1}. The error analysis done by Zistler et al. [76] suggested the major sources of error are the fitting process (≈14%) and the distance between electrodes (≈2%). In this study, the error in the value is estimated to be 16%. The resultant diffusion coefficient is $1.28 \pm 0.2 \times 10^{-5}$ cm^2 s^{-1}.

DC polarization

DC polarization measurement was also used to determine the bulk diffusion coefficient of I_3^- ions. The typical I-V curve is shown in **Fig.** 4.5, producing a limiting current density of

58.6 ±1.2 mAcm^{-2}. Based on **Eq.** 2.6, the diffusion coefficient D_{bulk} = 1.27 ±0.04 × 10^{-5} cm^2 s^{-1}, which bears good agreement with the value obtained from the EIS measurements, also with the value from existing literature (1.24 – 1.5 × 10^{-5} cm^{2}s^{-1}) [37, 86].

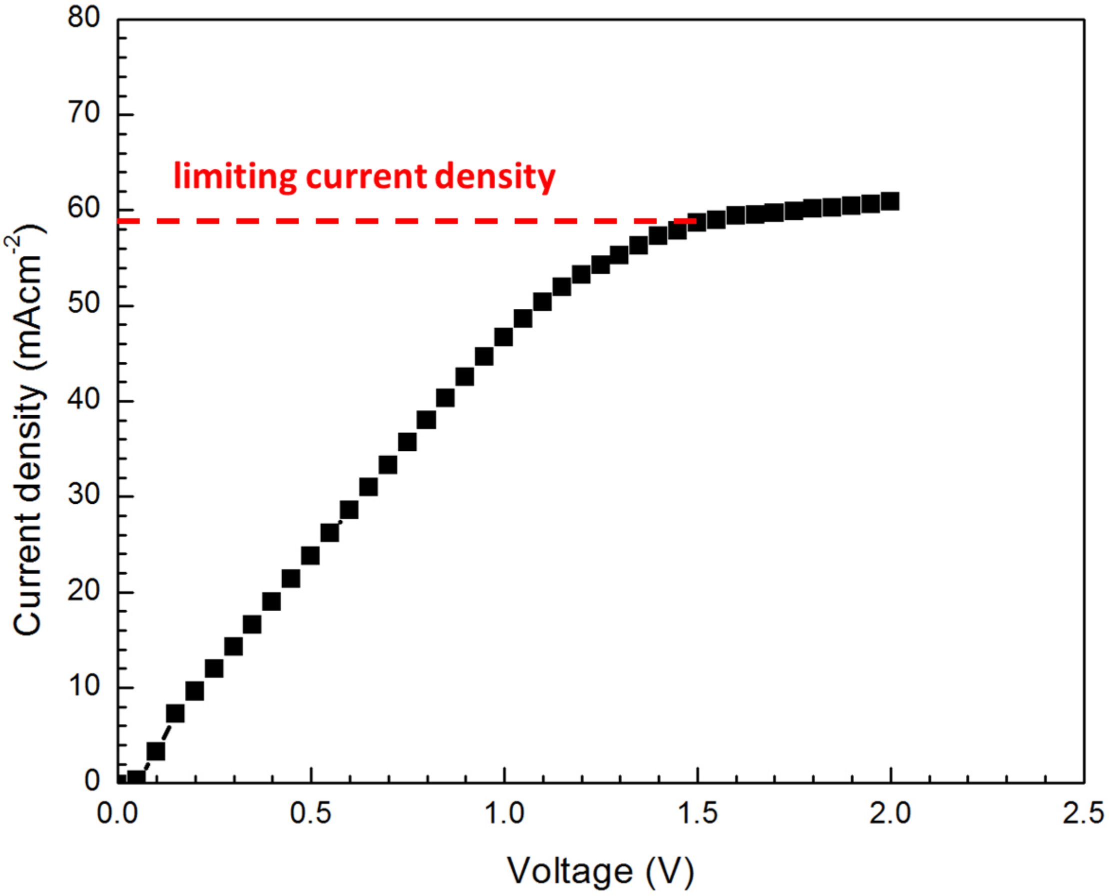

Figure 4.5: I-V characteristic curve of a sample device with only electrolyte

4.2.2 Measurement of Diffusion Coefficients in Mesoporous Films

The diffusion coefficients of I_3^- ions in TiO_2 mesoporous films with varying pore size were only measured by DC polarization tests, due to the limitations of impedance stated in section 2.3.2. The typical I-V characteristic curves of samples after 0 to 4 $TiCl_4$ treatments are shown in **Fig.** 4.6. The slopes of the curves represent the series resistance of the particular device, which may vary in each test. However, the current density at the plateau, which is the limiting current density, remained almost the same in samples after the same number of treatments. The further increase of current density after the plateau was due to the additional charge injection mechanism from the TiO_2 film into the redox system. It is the charge transfer process at the electrochemical junction formed between TiO_2 and the redox system under forward bias condition. Therefore, this charge injection mechanism exhibits a threshold voltage and was prohibited under low potential difference. It had no effect on the limiting current density measurement and would not interfere with the diffusion coefficient measurements.

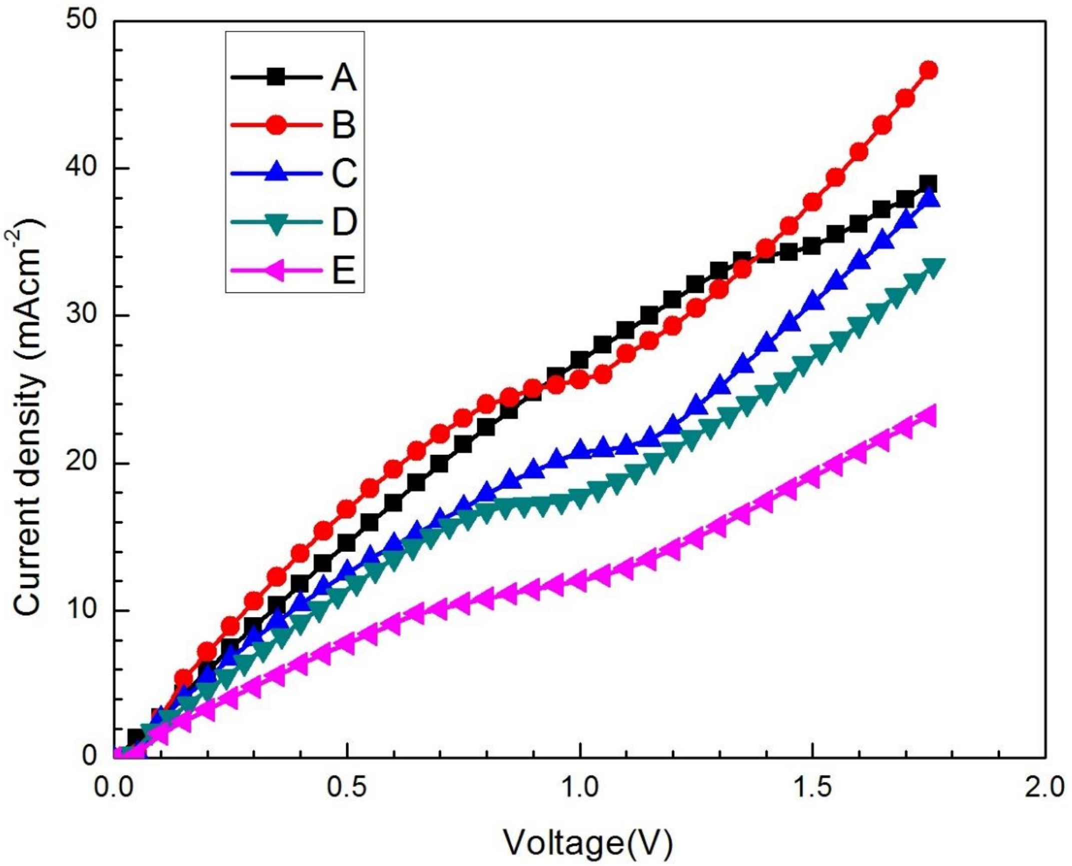

Figure 4.6: The typical I-V characteristic curves of sample devices with TiO_2 films after 0 to 4 $TiCl_4$ treatments

With the values of limiting current densities, as well as other necessary parameters available, which include bulk diffusion coefficient (D_{bulk}), film thickness, *t* and distance between electrodes, *l*, the diffusion coefficient in TiO_2 mesoporous film (D_{TiO2}) can be calculated from **Eq.** 2.9. The TiO_2 film thickness, *t* is 12 μm (Profilometer alpha step 200). The error of film thickness is not measured because the slight fluctuation on the surface has already been considered in the film porosity and its error. The distance between electrodes, *l* is the same as the thickness of the Surlyn sealing film. The Surlyn films were purchased as 25 μm. The thickness was measured again after purchase for confirmation, to be 24.8 ± 0.5 μm.

Referring to the error analysis from Zistler et al. [76], the major source of error is the distance between electrodes in their case, which was about 10% in the paper. However, in this study, the error of electrode distance is much smaller (≈2%). Considering the error in limiting current value as about 3%, the final error in the diffusion coefficient is only about 5% which is smaller than the error from impedance measurement.

Table 4.2: Comparison of effective diffusivities in TiO_2 (D_{TiO2}), normalized effective diffusivities (D_{eff}) and matrix factor (q) derived from the limiting current values

Sample	J_{lim} /mA cm^{-2}	D_{TiO2} /10^{-5} cm^2 s^{-1}	D_{eff} /10^{-5} cm^2 s^{-1}	Matrix Factor q [a]
A	35.25 ±1.25	0.747 ±0.038	1.22 ±0.09	1.05 ±0.11
B	24.80 ±0.60	0.513 ±0.016	1.03 ±0.05	1.24 ±0.09
C	21.10 ±0.45	0.437 ±0.012	1.08 ±0.07	1.18 ±0.11
D	16.67 ±0.35	0.343 ±0.009	1.01 ±0.05	1.26 ±0.10
E	10.33 ±0.50	0.207 ±0.011	0.721 ±0.055	1.78 ±0.18

[a] Apparent matrix factor values were calculated assuming absence of steric hindrance effect or any forms of diffusion other than pore diffusion. These values are for comparison purposes only and do not hold true in sample A and E.

The values of limiting current densities with respect to the samples after different numbers of $TiCl_4$ treatments are listed in the 2nd column of Table 4.2. The third column is the corresponding triiodide diffusion coefficients in the porous film from calculations. Based on **Eq.** 2.2, even in the pore-size independent diffusion region, the diffusion coefficients in the matrix would be affected by porosity. In order to make meaningful comparison, it is necessary to normalize these diffusion coefficients in the matrix with the porosity values of the TiO_2 films. The normalized effective diffusion coefficients (D_{eff}) of triiodide ions are given in the 4th column. The normalized effective diffusion coefficients are expected to remain constant in the pore size independent region, as shown in **Eq.** 4.1,

$$D_{eff} = \frac{D_{TiO2}}{\varepsilon} = \frac{D_{bulk}}{q} \tag{4.1}$$

The apparent matrix factors (5th column) could be derived from **Eq.** 4.1. These are called apparent matrix factors because they might not be the true matrix factors of the sample if the diffusion in the particular sample is not in the range of pore-size independent diffusion. The apparent matrix factors will be used as important reference in further discussion.

4.3 PORE-SIZE DEPENDENCE OF TRIIODIDE ION DIFFUSIVITY

The pore-size dependence of triiodide ion diffusivity in dye-sensitized solar cells can be analyzed by plotting the effective diffusion coefficients (D_{eff}) against the average pore diameters of the sample films, as shown in **Fig.** 4.7. The horizontal and vertical error bars of each point were carried forward from Table 4.1 and 4.2 respectively.

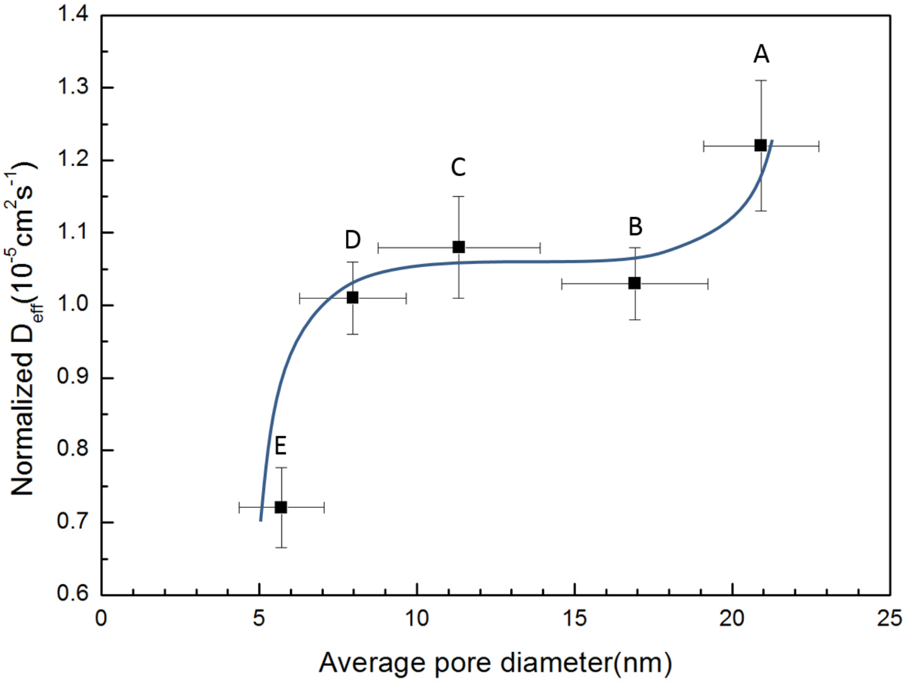

Figure 4.7: The trend of normalized diffusivities corresponding to the changing average pore diameters. Points A to E represent samples after 0 to 4 $TiCl_4$ treatments

The graph above can be divided into three distinct segments, viz., the plateau formed by sample B C and D, the decrease of diffusivity from sample D to E, and the unexpected increase of diffusivity from sample B to A. The implication of each segment will be discussed in detail in the following sections.

4.3.1 Pore-size Independent Region

The plateau formed by sample B C D is a strong evidence of the region of pore size independent diffusion. It ranges from average pore diameter larger than 5-7 nm. In this region, the mean free path of collision of I_3^- ions is much smaller than the pore diameter formed between TiO_2 nanoparticles. Similar to bulk diffusion, most of the collisions happen between liquid molecules. The overall diffusion coefficient in TiO_2 porous film (D_{TiO2}) is only affected by porosity and matrix factor.

The matrix factors of the three points are similar, which is about 1.23 on average. This value is in good agreement with the matrix factor of monodispersed random sphere packing (i.e., 1.2 to 1.8) acquired from theoretical modelling and calculation [59]. This further proves that the ion diffusivities in these three samples follow the pore-size independent diffusion described by **Eq.** 2.2, as well as the prediction from Kärger [31].

4.3.2 Pore-size Dependent Region

The decrease of effective diffusion coefficient from sample D to sample E symbolizes the region of pore-size dependent diffusion. It covers the range of average pore diameter smaller than 5-7 nm. In this region, the steric hindrance effect of pore wall becomes noticeable, which means the overall mean free path of collision of I_3^- ions is significantly affected by the frequent collisions between the triiodide ions and the pore wall of TiO_2 matrix. The large difference of the diffusion coefficients between sample D and E shows that ion diffusivity is heavily dependent on the pore-size. This observation is consistent with the typical trend of exponential decrease of diffusivity with respect to pore-size in previous literature [61].

The matrix factor of sample E is 1.78, which is exceptionally higher than the rest. However, the matrix factor of all the samples are expected to be similar. Thus, this value is not the true matrix factor of the TiO_2 film. It simply implies that **Eq.** 2.2 is no longer applicable in this sample and the diffusion is not pore-size independent anymore.

Although there is only one point showing impeded diffusion with respect to the plateau formed by samples B, C and D, the decrease of diffusivity from sample D to E was evident. It was substantiated by repeated measurements. It might seem to be more convincing with additional data points in the region of pore-size dependent diffusion. However, there is insufficient room between point D and E, as the error bars of these two data points already overlap with each other. It is also unrealistic to further decrease the average pore diameter of the mesoporous film by $TiCl_4$ treatments, because in that case the error in pore diameter would be comparable to the pore-size itself, resulting in unreliable measurement results.

4.3.3 Transition and Unification of Two Opposite Diffusion Patterns

Based on the trend described in **Fig.** 4.7, there exists a rather sharp transition between pore-size dependent and independent diffusion regions. The transition is located in the range of 5-7 nm. The size of I_3^- ions is estimated to be about 550-580 pm [87]. Therefore, the λ value at the transition closely approximates 0.1, which bears remarkable agreement to the theoretical prediction [31]. One possible explanation for this observation is the lack of interaction or bonding process between the non-polar triiodide ions and the passivated TiO_2 surface after $TiCl_4$ treatments [81].

The sharp transition of triiodide diffusion patterns in dye-sensitized solar cells was confirmed for the first time. The results demonstrated the co-existence of two opposite kinds of diffusion patterns with their respective valid regimes. Furthermore, as mentioned earlier, various fabrication processes, such as one-step $TiCl_4$ post-treatment and dye loading, will lead to a decrease of average pore diameter. The amount of shrinkage is estimated to be 5-10 nm in total [69, 70]. Based on the range of pore-size independent diffusion, it can be concluded that these processes are most likely to only shift the pore-size in the range of pore-size independent diffusion and would not lead to the transition to pore-size dependent diffusion. Therefore, the limiting current density would be little affected by these processes, and only from the effect of porosity decrease. This conclusion is very meaningful in the design of device structure by predicting the limiting current density, so as to prevent the mass transport rate of ions from becoming the limiting factor of overall device performance.

4.4 SURFACE DIFFUSION IN UNTREATED TiO_2 FILM

The increase of diffusivity from sample B to A was surprising because the normalized effective diffusivities are expected to be constant above the point of transition. The suggested explanation of this unexpected increase is the involvement of additional diffusion mechanism in sample A, i.e. surface diffusion.

It is noteworthy that the value of matrix factor of sample A is unrealistically low (≈1.05). A matrix factor close to unity means the tortuosity and constrictivity of the porous structure both approximate 1. A tortuosity factor of 1 suggests the path between any two points in the porous matrix equals to the straight line distance between them, which is impossible in a mesoporous film [59]. The calculation of matrix factor was based on the assumption of absence of any additional mechanisms which may affect the overall diffusion rate. Therefore, an unrealistically low matrix factor actually implies the involvement of additional diffusion mechanism which fastens the overall mass transport rate.

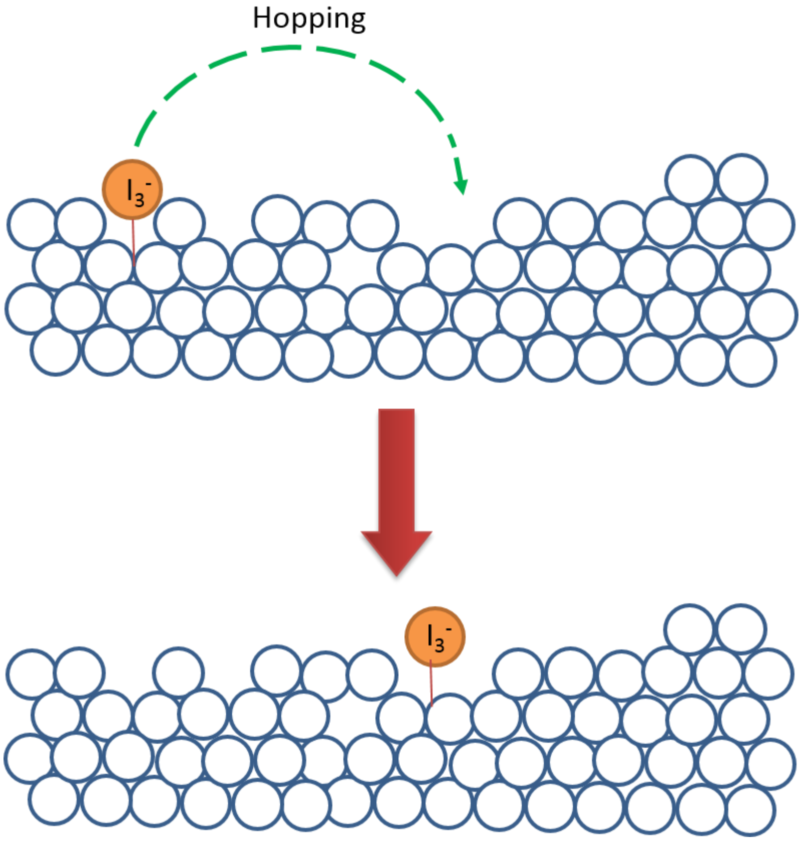

Figure 4.8: Illustration of hopping mechanism of adsorbed molecules during surface diffusion

Surface diffusion is a hopping mechanism of surface adsorbed molecules between adsorption sites (**Fig.** 4.8). It is more common in gas diffusion, but also observed in liquid cases [62, 88]. The relationship between the overall diffusion coefficient and surface diffusion coefficient is expressed as **Eq.** 4.2.

$$D_{total} = D_{pore} + \frac{1-\varepsilon_p}{\varepsilon_p} k D_{surface} \quad k\text{: adsorption constant} \qquad (4.2)$$

Surface diffusion is the soundest explanation for the deviation in sample A, because the major difference between sample A and any other samples is that sample A did not undergo any $TiCl_4$ treatment. It reasonable to deduce that the surface modification resulted from the epitaxial growth of TiO_2 could have acted as a surface passivation process, and considerably reduced the available adsorption sites [41]. The adsorption constant, k would be decreased. Therefore, the effect of surface diffusion is only perceptible in untreated TiO_2 thin film.

5 CONCLUSION

In this study, the diffusion patterns of triiodide ions in TiO_2 films of variable pore-size were investigated using electrochemical tests. The variation of average pore diameter of the mesoporous TiO_2 film was successfully achieved by epitaxial coverage of TiO_2 from $TiCl_4$ treatments, and validated by the nitrogen isotherm characterization. The results show the presence of both pore-size dependent and independent diffusion in the target range, separated by a sharp transition. The critical point of transition was located in the range of 5-7 nm. Two opposite views regarding the pore size dependence of liquid diffusion behavior in mesopores are now both accommodated under the same scheme of dye-sensitized solar cells.

Furthermore, the resultant trend of triiodide ion diffusion is highly consistent with the theoretical prediction, in the absence of frequently observed impeded diffusion in mesopores in other systems. The range of pore-size independent diffusion exclude the possibility of severe hindrance effect which might be brought by the dye loading and one-step $TiCl_4$ treatment during cell fabrication.

More importantly, my finding is extremely meaningful in the prediction of mass transfer limited current of the device and therefore the optimization of the device efficiency. In dye-sensitized solar cells, smaller pore-size is ideal for maximizing the surface area of TiO_2 thin film, which facilitates dye loading and thus light harvesting. However, smaller pores may have adverse effect on the mass transport rate. Based on the results of this study, it is possible to find the minimum pore-size without hindering the mass transport rate. The optimization between surface area and mass transport rate could be accomplished.

The surprisingly high limiting current density in sample A with untreated TiO_2 thin film suggests the involvement of additional diffusion mechanism, i.e., surface diffusion. At the same time, the experiment observation indicates that this mechanism will be suppressed by the surface modification of $TiCl_4$ treatments. Therefore, in spite of the improvements of overall cell efficiency brought by the $TiCl_4$ post-treatment, it might have detrimental effect on the mass transport rate of ions.

BIBLIOGRAPHY

[1] J.F. Bookout, Two Centuries of Fossil Fuel Energy, in: International Geological Congress, Washington DC, 1985.

[2] BP, Statistical Review of World Energy 2009, in, 2009.

[3] A. Goetzberger, C. Hebling, H.W. Schock, Mater. Sci. Eng. R-Rep., 40 (2003) 1-46.

[4] D.M. Chapin, C.S. Fuller, G.L. Pearson, J. Appl. Phys., 25 (1954).

[5] A. Blakers, Fertkorperprobleme-Adv. Solid State Phys., 30 (1990) 403-423.

[6] Antonio Luque, S. Hegedus, Handbook of Photovoltaic Science and Engineering, 2nd ed., Wiley, 2011.

[7] P.T. Landsberg, P. Baruch, J. Phys. A-Math. Gen., 22 (1989) 1911-1926.

[8] W. Shockley, H.J. Queisser, J. Appl. Phys., 32 (1961).

[9] H. Hoppe, N.S. Sariciftci, J. Mater. Res., 19 (2004) 1924-1945.

[10] K.K. Chong, S.L. Lau, T.K. Yew, P.C.L. Tan, Renew. Sust. Energ. Rev., 19 (2013) 598-612.

[11] J.F. Geisz, D.J. Friedman, J.S. Ward, A. Duda, W.J. Olavarria, T.E. Moriarty, J.T. Kiehl, M.J. Romero, A.G. Norman, K.M. Jones, Appl. Phys. Lett., 93 (2008) 3.

[12] Ncouniot, Structure of a MJ Solar cell, in, Fraunhofer Institute for Solar Energy Systems, 2010.

[13] Y. Rosenwaks, M.C. Hanna, D.H. Levi, D.M. Szmyd, R.K. Ahrenkiel, A.J. Nozik, Physical Review B, 48 (1993) 14675-14678.

[14] A.J. Nozik, Nat. Nanotechnol., 4 (2009) 548-549.

[15] NREL, Best research photovoltaic cell efficiencies, in, US Department of Energy, 2012.

[16] B. Oregan, M. Grätzel, Nature, 353 (1991) 737-740.

[17] A. Yella, H.W. Lee, H.N. Tsao, C.Y. Yi, A.K. Chandiran, M.K. Nazeeruddin, E.W.G. Diau, C.Y. Yeh, S.M. Zakeeruddin, M. Grätzel, Science, 334 (2011) 629-634.

[18] M. Grätzel, J. Photochem. Photobiol. A-Chem., 168 (2004) 235-235.

[19] L. Deng, Dye-sensitized solar cells with a solid hole conductor, in: Materials Science and Engineering, McMaster University, Hamilton, 2012.

[20] M. Saito, S. Fujihara, Energy Environ. Sci., 1 (2008) 280-283.

[21] E.A. Gibson, A.L. Smeigh, L. Le Pleux, J. Fortage, G. Boschloo, E. Blart, Y. Pellegrin, F. Odobel, A. Hagfeldt, L. Hammarstrom, Angew Chem Int Edit, 48 (2009) 4402-4405.

[22] S.A. Haque, E. Palomares, B.M. Cho, A.N.M. Green, N. Hirata, D.R. Klug, J.R. Durrant, J Am Chem Soc, 127 (2005) 3456-3462.

[23] Q.B. Meng, K. Takahashi, X.T. Zhang, I. Sutanto, T.N. Rao, O. Sato, A. Fujishima, H. Watanabe, T. Nakamori, M. Uragami, Langmuir, 19 (2003) 3572-3574.

[24] J. Kruger, R. Plass, L. Cevey, M. Piccirelli, M. Grätzel, U. Bach, Appl. Phys. Lett., 79 (2001) 2085-2087.

[25] J.K. Koh, J. Kim, B. Kim, J.H. Kim, E. Kim, Advanced Materials, 23 (2011) 1641-+.

[26] T. Hoshikawa, T. Ikebe, R. Kikuchi, K. Eguchi, Electrochim. Acta, 51 (2006) 5286-5294.

[27] J.J. Nelson, T.J. Amick, C.M. Elliott, J. Phys. Chem. C, 112 (2008) 18255-18263.

[28] P. Wachter, M. Zistler, C. Schreiner, M. Berginc, U.O. Krasovec, D. Gerhard, P. Wasserscheid, A. Hinsch, H.J. Gores, J. Photochem. Photobiol. A-Chem., 197 (2008) 25-33.

[29] G.P. Kalaignan, Y.S. Kang, J. Photochem. Photobiol. C-Photochem. Rev., 7 (2006) 17-22.

[30] A. Hagfeldt, G. Boschloo, L. Sun, L. Kloo, H. Pettersson, Chemical Reviews, 110 (2010) 6595-6663.

[31] J. Kärger, D.M. Ruthven, Diffusion in zeolites and other microporous solids, in, : Wiley, New York, 1992.

[32] I. Jerman, V. Jovanovski, A.S. Vuk, S.B. Hocevar, M. Gaberscek, A. Jesih, B. Orel, Electrochim. Acta, 53 (2008) 2281-2288.

[33] d. Grotthuss, Ann. Chim., 58 (1806) 54-73.

[34] R. Kawano, M. Watanabe, Chem. Commun., (2005) 2107-2109.

[35] J. Rouquerol, D. Avnir, C.W. Fairbridge, D.H. Everett, J.H. Haynes, N. Pernicone, J.D.F. Ramsay, K.S.W. Sing, K.K. Unger, Pure Appl. Chem., 66 (1994) 1739-1758.

[36] G. Kron, U. Rau, M. Durr, T. Miteva, G. Nelles, A. Yasuda, J.H. Werner, Electrochem. Solid State Lett., 6 (2003) E11-E14.

[37] A. Hauch, A. Georg, Electrochim. Acta, 46 (2001) 3457-3466.

[38] G.-J. Yang, C.-J. Li, S.-Q. Fan, J.-C. Gao, Surface & Coatings Technology, 205 (2011) 3205-3210.

[39] J. Maier, Journal of Power Sources, 174 (2007) 569-574.

[40] J.B. Wagner, Materials Research Bulletin, 15 (1980) 1691-1701.

[41] N.N. Bwana, Nano Res., 1 (2008) 483-489.

[42] F.Y. Li, L. Zhang, R.M. Metzger, Chemistry of Materials, 10 (1998) 2470-2480.

[43] G.K. Mor, K. Shankar, M. Paulose, O.K. Varghese, C.A. Grimes, Nano Letters, 5 (2005) 191-195.

[44] G.K. Mor, O.K. Varghese, M. Paulose, K. Shankar, C.A. Grimes, Solar Energy Materials and Solar Cells, 90 (2006) 2011-2075.

[45] K. Shankar, J. Bandara, M. Paulose, H. Wietasch, O.K. Varghese, G.K. Mor, T.J. LaTempa, M. Thelakkat, C.A. Grimes, Nano Letters, 8 (2008) 1654-1659.

[46] J.R. Jennings, A. Ghicov, L.M. Peter, P. Schmuki, A.B. Walker, J Am Chem Soc, 130 (2008) 13364-13372.

[47] M. Zukalova, A. Zukal, L. Kavan, M.K. Nazeeruddin, P. Liska, M. Grätzel, Nano Letters, 5 (2005) 1789-1792.

[48] C.J. Brinker, Y.F. Lu, A. Sellinger, H.Y. Fan, Advanced Materials, 11 (1999) 579-+.

[49] M.K. Nazeeruddin, P. Pechy, M. Grätzel, Chem. Commun., (1997) 1705-1706.

[50] M.K. Nazeeruddin, P. Pechy, T. Renouard, S.M. Zakeeruddin, R. Humphry-Baker, P. Comte, P. Liska, L. Cevey, E. Costa, V. Shklover, L. Spiccia, G.B. Deacon, C.A. Bignozzi, M. Grätzel, J Am Chem Soc, 123 (2001) 1613-1624.

[51] M.K. Nazeeruddin, A. Kay, I. Rodicio, R. Humphrybaker, E. Muller, P. Liska, N. Vlachopoulos, M. Grätzel, J Am Chem Soc, 115 (1993) 6382-6390.

[52] K. Hara, Y. Dan-Oh, C. Kasada, Y. Ohga, A. Shinpo, S. Suga, K. Sayama, H. Arakawa, Langmuir, 20 (2004) 4205-4210.

[53] T. Horiuchi, H. Miura, S. Uchida, Chem. Commun., (2003) 3036-3037.

[54] N. Papageorgiou, Y. Athanassov, M. Armand, P. Bonhote, H. Pettersson, A. Azam, M. Grätzel, Journal of the Electrochemical Society, 143 (1996) 3099-3108.

[55] Y. Bai, Y. Cao, J. Zhang, M. Wang, R. Li, P. Wang, S.M. Zakeeruddin, M. Graetzel, Nat. Mater., 7 (2008) 626-630.

[56] W. Kubo, K. Murakoshi, T. Kitamura, Y. Wada, K. Hanabusa, H. Shirai, S. Yanagida, Chem. Lett., (1998) 1241-1242.

[57] P. Wang, S.M. Zakeeruddin, J.E. Moser, M.K. Nazeeruddin, T. Sekiguchi, M. Grätzel, Nat. Mater., 2 (2003) 498-498.

[58] M.G. Kang, K.M. Kim, K.S. Ryu, S.H. Chang, N.G. Park, J.S. Hong, K.J. Kim, Journal of the Electrochemical Society, 151 (2004) E257-E260.

[59] J.v. Brakel, P.M. Heertjes, Int. J. Heat Mass Transf., 17 (1974) 1093-1103.

[60] M.A. Winkler, Chemical Engineering Problems in Biotechnology, Springer, New York, 1990.

[61] A. Mitzithras, F.M. Coveney, J.H. Strange, J. Mol. Liq., 54 (1992) 273-281.

[62] N. Koone, Y. Shao, T.W. Zerda, J. Phys. Chem., 99 (1995) 16976-16981.

[63] C.N. Satterfield, M.W. Vaneek, G.S. Bliss, Aiche J., 24 (1978) 709-717.

[64] B.D. Prasher, Y.H. Ma, Aiche J., 23 (1977) 303-311.

[65] T.K. Yun, S.S. Park, D. Kim, Y.-K. Hwang, S. Huh, J.Y. Bae, Y.S. Won, Journal of Power Sources, 196 (2011) 3678-3682.

[66] W. Chen, Y. Qiu, K. Yan, S. Yang, Journal of Power Sources, 196 (2011) 10806-10816.

[67] S. Moribe, A. Takeichi, J. Seki, N. Kato, K. Higuchi, K. Ueyama, K. Mizumoto, T. Toyoda, Appl. Phys. Express, 5 (2012) 3.

[68] J.Y. Kim, K.J. Lee, S.H. Kang, J. Shin, Y.E. Sung, J. Phys. Chem. C, 115 (2011) 19979-19985.

[69] P.M. Sommeling, B.C. O'Regan, R.R. Haswell, H.J.P. Smit, N.J. Bakker, J.J.T. Smits, J.M. Kroon, J.A.M. van Roosmalen, J. Phys. Chem. B, 110 (2006) 19191-19197.

[70] N. Papageorgiou, C. Barbe, M. Grätzel, J. Phys. Chem. B, 102 (1998) 4156-4164.

[71] J. Bisquert, J. Phys. Chem. B, 106 (2002) 325-333.

[72] J. Bisquert, D. Cahen, G. Hodes, S. Ruhle, A. Zaban, J. Phys. Chem. B, 108 (2004) 8106-8118.

[73] J. Bisquert, V.S. Vikhrenko, J. Phys. Chem. B, 108 (2004) 2313-2322.

[74] S. Phadke, A. Du Pasquier, D.P. Birnie, III, J. Phys. Chem. C, 115 (2011) 18342-18347.

[75] Q. Wang, J.E. Moser, M. Grätzel, J. Phys. Chem. B, 109 (2005) 14945-14953.

[76] M. Zistler, P. Wachter, P. Wasserscheid, D. Gerhard, A. Hinsch, R. Sastrawan, H.J. Gores, Electrochim. Acta, 52 (2006) 161-169.

[77] V. Freger, Electrochem. Commun., 7 (2005) 957-961.

[78] S. Ito, T.N. Murakami, P. Comte, P. Liska, C. Grätzel, M.K. Nazeeruddin, M. Grätzel, Thin Solid Films, 516 (2008) 4613-4619.

[79] L. Kavan, M. Grätzel, Electrochim. Acta, 40 (1995) 643-652.

[80] B.C. O'Regan, J.R. Durrant, P.M. Sommeling, N.J. Bakker, J. Phys. Chem. C, 111 (2007) 14001-14010.

[81] F.J. Knorr, D. Zhang, J.L. McHale, Langmuir, 23 (2007) 8686-8690.

[82] N. Hwang, A.R. Barron, Schematic representation of the BET instrument, in, 2011.

[83] S. Brunauer, L.S. Deming, W.E. Deming, E. Teller, J. Am. Chem. Soc., 62 (1940) 1723.

[84] S. Brunauer, P.H. Emmett, E. Teller, J. Am. Chem. Soc., 60 (1938) 309.

[85] E.P. Barrett, L.G. Joyner, P.P. Halenda, J. Am. Chem. Soc. , 73 (1951) 373-380.

[86] V.A. Macagno, M.C. Giordano, A.J. Arvia, Electrochim. Acta, 14 (1969) 335.

[87] D. Shriver, P. Atkins, Inorganic Chemistry, W.H. Freeman & Company, 2010.

[88] R. McHardy, W.H. Haiss, R.J. Nichols, PCCP Phys. Chem. Chem. Phys., 2 (2000) 1439-1444.